Slab tearing and delamination of the Indian lithospheric mantle during flat-slab subduction, southeast Tibet

Lin Liu[1], Danian Shi[2], Simon L Klemperer[3], and Jianyu Shi[4]

[1]Affiliation not available
[2]Chinese Academy of Geological Sciences
[3]Department of Geophysics, Stanford University
[4]National Marine Environmental Forecasting Center

November 14, 2023

Slab tearing and delamination of the Indian lithospheric mantle during flat-slab subduction, southeast Tibet

Lin LIU,[1*] Danian SHI,[2] Simon L. KLEMPERER,[3*] Jianyu SHI[4]

[1]Frontiers Science Center for Deep Ocean Multispheres and Earth System, Key Lab of Submarine Geosciences and Prospecting Techniques, MOE and College of Marine Geosciences, Ocean University of China, 266100 Qingdao, China;

[2]Chinese Academy of Geological Sciences, 100037 Beijing, China;

[3]Department of Geophysics, Stanford University, Stanford, CA 94305-2215;

[4]National Marine Environmental Forecasting Center, Beijing 100081, China

[*]To whom correspondence may be addressed: Simon L. KLEMPERER; Lin LIU

Email: sklemp@stanford.edu; liulin1991@ouc.edu.cn

Abstract

The first-order configuration of the Himalayan orogen is defined by the northward motion of the Indian Plate, whether directly "underplating" under the Tibetan crust or "subducting" beneath a mantle wedge. Our 3D S-wave receiver-functions newly reveal orogen-perpendicular tearing or warping of the Indian Plate. West of 90°E, the southern limit of the Tibetan lithosphere-asthenosphere boundary is at the Indian crustal front, ~100-km north of the Yarlung-Zangbo suture, implying an underplating of the intact Indian lithosphere beneath Tibet. Further east, the delaminated Indian lithospheric mantle during its gravitationally-induced rollback is separated from the Indian crust by an interposed asthenospheric wedge. The nascent Tibetan lithosphere and its subjacent thin asthenosphere continue ~100 km south of the Yarlung-Zangbo suture. This contrast in lithospheric structures across the Yadong-Gulu and Cona-Sangri rifts at 90–92°E, in

agreement with helium isotopic anomalies and deep seismicity, requires the subducting Indian Plate be warped or torn.

1. Introduction

Continental collision on Earth is today best expressed in the Himalaya and the Tibet Plateau that are a consequence of collision of India and Asia since 60 Ma (Kapp and DeCelles, 2019). To understand the geodynamic processes of continental collision we must characterize the lithospheric architecture (Dal Zilio et al., 2021). Arguments from crustal and mantle density suggest Indian continental lithosphere should greatly resist subduction unless overlying crust is separated from the mantle lithosphere (Capitanio et al., 2010). Accurate locations of the crustal front (northern limit of Indian crust beneath Tibet) and the mantle suture (southern limit of Tibetan mantle at the Moho) (Jin et al., 1996) with respect to the surface Yarlung-Zangbo suture (YZS) (Fig. 1), are needed to define the 3D geometry of the India-Asian collision zone, and determine whether Indian crust subducts with Indian mantle lithosphere or detaches and is incorporated into the Tibetan crust. End-member hypotheses largely driven by contradictory seismic-tomography interpretations – sub-horizontal underplating of India beneath Tibet (Barazangi and Ni, 1982; McKenzie et al., 2019) vs. steep subduction of India beneath southernmost Tibet (Li et al., 2008; Wang et al., 2022) – gloss over growing evidence for west-east variability in lithospheric structure (Chen et al., 2017; Liang et al., 2016; Nunn et al., 2014). The diverse tomographic models of our study region of southeast Tibet include high-wavespeed regions interpreted as

underthrust Indian cratonic lithosphere (Chen et al., 2017), and localized lower-wavespeed regions interpreted as showing asthenospheric upwelling (Ren and Shen, 2008) or lithospheric removal by Rayleigh-Taylor instability (Nunn et al., 2014) or fragmentation of the Indian plate along north-south breaks (Liang et al., 2016) or sub-Moho thin layers with partial melt (Chen et al., 2017). However, tomographic models are invariably smoothed and although synthetic tests demonstrate good recovery of structures with diameter 150–200 km these models cannot recover sharp changes or small-scale reversals in the velocity-depth profile (Chen et al., 2017; Liang et al., 2016; Nunn et al., 2014; Ren and Shen, 2008). Hence the detailed upper-mantle geometry of continental collision is widely studied, as in this paper, using receiver functions.

P-wave seismic receiver functions (PRFs, P-to-S conversions at lithospheric wavespeed boundaries) image Indian underthrust crust as a 'seismic doublet' (Kind et al., 2002; Nábělek et al., 2009; Shi et al., 2015) or as a crustal thickness change (Wang et al., 2019) at its northern limit at the crustal front, approximately 200-km north of the YZS. PRFs show the Moho at 60–80 km depth north of the YZS (Kind et al., 2002; Nábělek et al., 2009; Shi et al., 2020; Shi et al., 2015) but deeper boundaries such as the lithosphere-asthenosphere boundary (LAB) are largely obscured by multiply-converted phases so that S-receiver functions (SRFs) are now commonly used to locate the LAB (Rychert et al., 2020). The LAB in the east-central India-Tibet collision zone has been extensively studied with SRF imaging (Devi et al., 2011; Hu et al., 2015; Kumar et al., 2006; Liu et al., 2020; Shi et al., 2015; Xu et al., 2021; Xu et al., 2013; Zhao et al., 2011) resulting in confusion because of the weak response of the LAB, as compared to the easily resolved Moho, that has led to subjective and conflicting interpretations of negative velocity gradients (NVGs)

that typically fall into two depth ranges, shallow at <~125 km (Shi et al., 2015; Xu et al., 2021) (Fig. S1a), and deep at >~170 km (Devi et al., 2011; Kumar et al., 2006) (Fig. S1b,c). Different authors claim to image the Indian LAB (I-LAB), the Tibetan LAB (T-LAB), the Asian LAB (A-LAB) or even all three (Fig. S1). Some studies identified a north- or NNE-dipping NVG converter spanning the two depth ranges (Devi et al., 2011; Hu et al., 2015; Zhao et al., 2010; Zhao et al., 2011) (Fig. S1b, d), interpreted as north-dipping I-LAB and consistent with shallower north-dipping positive converters interpreted as top of subducting Indian lithosphere (Fig. S1e). Contradictory results are due to the use of different data, different processing [e.g. lower (Kumar et al., 2006) or higher (Xu et al., 2013) frequency bands] and different picking schemes [sometimes every negative oscillation (Xu et al., 2013), sometimes a smoothed line through the larger amplitudes (Kumar et al., 2006)] leading to picks that can differ by >50 km vertically in the same location (e.g. west-center of Fig. S1).

Even where there is agreement on depths to specific negative wavespeed gradients, interpretations often differ. Shallow NVGs are typically identified as T-LAB north of the YZS but as I-LAB further south (Xu et al., 2021; Xu et al., 2013) (Fig. S1a). Deeper NVGs are interpreted as A-LAB when further north, or I-LAB when further south(Kumar et al., 2006) (Fig. S1b). The dependence of interpretations on pre-conceived geometric models is highlighted by conflicting interpretations of the same converter [e.g. I-LAB (Devi et al., 2011; Kumar et al., 2006) of Fig. S1b is in part A-LAB (Xu et al., 2013) of Fig. S1c] and by the same interpretation of different converters [e.g. I-LAB (Xu et al., 2021) in Fig. S1a is >100 km shallower than I-LAB (Kumar et al., 2006) in Fig. S1b].

Shear-wave splitting (SWS) provides an alternative view of plate geometry beneath Tibet through orientation of fast polarization direction (FPD) and differential travel-times (dt) of fast and slow waves due to receiver-side anisotropy of teleseismic S-phases. The mantle suture and Indian mantle front have been interpreted from northward (across-strike) increases in split times and coherence of FPD (Chen and Özalaybey, 1998) though there is also along-strike variability in these parameters (Chen et al., 2010) (Fig. 1b). Asthenospheric flow and lithospheric fabrics (either or both) that wrap circumferentially around the Eastern Himalayan Syntaxis (EHS) have been inferred from the circumferential pattern of anisotropy parallel to the Bangong-Nujiang (BNS) and Jinsha River sutures (JRS) (Liu et al., 2019; Wang et al., 2008) that contrasts with the spatially inconsistent and often weaker azimuthal anisotropy typical of the Tethyan Himalaya (Chen et al., 2010) (Fig. 1b). Only limited numbers of earthquakes have appropriate source depths and offsets to allow clear estimation of SWS parameters, and numerous stations only yield 'null' SWS results (no measurable anisotropy, whether due to a transversely-isotropic mantle and crust, or to anisotropy that is aligned parallel or perpendicular to the back-azimuth from recording station to studied earthquake).

Here we present first SRF and SWS results from 94 broadband seismic stations deployed west-east across southern Tibet, for which only PRF results were previously published (Shi et al., 2020), combined with our re-analysis of available older data. We use auto-picking of old and new SRF data to objectively map the LAB (Figs. 1a, 2) and define the region of the Tibetan Plateau directly underlain by Indian lithospheric mantle. Further north and east, across a boundary corroborated using SWS results (Figs. 1b, 3), we show evidence for a thin Tibetan mantle-lithosphere. Our geometric model is consistent with

mid-Tertiary Indian slab break-off (Craig et al., 2020), the northern limit of intermediate-depth earthquakes above and below the Moho (Priestley et al., 2008; Song and Klemperer, 2023), the southern limit of ³He-enriched thermal waters (Klemperer et al., 2022), and patterns of NNE-trending grabens, normal-faulting and upper-crustal-earthquake mechanisms (Copley et al., 2011) (Fig. 4a).

2. Data and Methods

2.1. Data Processing for S-Receiver Functions

The Sp phase (teleseismic S converted at a receiver-side wavespeed discontinuity or gradient to an upward travelling P wave) arrives prior to, and its reverberations arrive later than, the S phase (Faber and Müller, 1980; Liu and Gao, 2018). Thus SRFs are free of contaminating energy that bedevils PRFs, and the LAB is usually better detected by SRFs than by PRFs (Faber and Müller, 1980; Liu and Gao, 2018). We used teleseismic events with magnitudes >5.0 and epicentral distances of 55–170° (Fig. S9a) to calculate SRFs for all available stations shown in Fig. S1 (Kumar et al., 2006; Shi et al., 2015; Zhao et al., 2010; Zhao et al., 2011) as well as newer recordings (Shi et al., 2020). Some published Indian and Chinese data (Devi et al., 2011; Hu et al., 2015; Liu et al., 2020; Xu et al., 2021; Xu et al., 2013) were not available for re-analysis.

We rotated three-component ZNE seismograms into LQT co-ordinates using theoretical back-azimuth and incident angles (Kind et al., 2012), keeping seismograms with signal-to-noise ratio >1.5 measured as the ratio of Sp to direct-S wave on the Q component. We time-reversed all traces so that Sp phases follow the direct S wave. SRFs were calculated using an iterative time-domain code (Ammon, 1991) to deconvolve the L

component by the S signal on the Q component (Kind et al., 2012), and a Gaussian filter width alpha=1.5 (effective frequencies ~0.01–0.5 Hz). We used two additional stages of data selection based on cross-correlation coefficients (XCC) between each station-averaged SRF and its individual SRFs for 0 to 30 sec after direct S. We retained only SRFs with XCC ≥0.3, then re-stacked the remaining SRFs, re-calculated XCC, and retained only SRFs with XCC ≥0.7. Of the initial 11,096 SRFs, we retained 4,051 high-quality SRFs from 244 events and 462 stations. We stacked moveout-corrected SRFs (Dueker and Sheehan, 1997) with 1/N normalization into 1°- and 0.5°-radius circular bins (with bin-center separations of 0.5°) based on the location of piercing points at 150 km depth calculated from the IASP91 Earth model (Fig. 1a). We converted from time to depth down to 300 km using IASP91 (Figs. 2, S3, S4). Relative depth uncertainty between different areas or depths of our model space is likely <10 km based on modelling (Gao and Liu, 2014) as wavespeed variability within SE Tibet is likely less than a few percent (e.g. Chen et al., 2017).

2.2. Data Processing for Shear-Wave Splitting

XKS (the generic term for PKS, SKKS and SKS) seismic phases emanate from an earthquake as P or S waves, remain as or convert to P as they cross the core-mantle boundary (CMB) into the outer core, then convert back to S as they exit the core to be recorded as S arrivals (Long and Silver, 2009; Savage, 1999). Anisotropy splits S phases into two waves with different wavespeeds and perpendicular polarizations, i.e., SWS (Fig. S10). The faster split wave is polarized parallel to the direction of maximum wavespeed in the anisotropic medium. SWS parameters (time delay dt between fast and slow waves and polarization direction ϕ of the fast wave or FPD) obtained from XKS measurements

represent the accumulated effect of the anisotropy of the medium along the ray propagation path from the CMB to the recording station (Long and Silver, 2009; Savage, 1999).

We used teleseismic events with magnitude >5.2 and epicentral distances 83–111° (SKS), 86–170° (SKKS) and 130–135° (PKS) (Fig. S9b). We used 95 earthquakes yielding 566 SKS, 137 SKKS and 7 PKS split measurements, with one to thirteen measurements averaged at each station. Our grid search identified the SWS parameters (FPD, dt) that correct the observed seismogram to minimize energy on the transverse component (Silver and Chan, 1991), i.e. characterize the single horizontal layer with simple horizontal anisotropy that best matches the data recorded at each station. When multiple observations are made at a single station, we average the results to obtain a single station-average measurement (Fig. S7). Station-average splitting times range from 0.2 to 2.25s.

2.3. Identification of Moho on SRFs

Almost all our summed SRF traces show a clear positive (red) converter at about 70 km depth (Figs 2c–j, S3, S4) as expected from numerous PRF studies that identify the Moho at this depth (Kind et al., 2002; Nábělek et al., 2009; Shi et al., 2020; Shi et al., 2015). PRFs, being higher frequency than SRFs, have better depth resolution and resolve a doublet converter interpreted as underthrust Indian crust at the base of the Tibetan crust (Kind et al., 2002; Nábělek et al., 2009; Shi et al., 2020; Shi et al., 2015). This doublet has been mapped from south of the YZS to its northern limit conventionally interpreted as the Indian crustal front north of the YZS (Kind et al., 2002; Nábělek et al., 2009; Shi et al., 2020; Shi et al., 2015) (Fig. 4a).

2.4. Identification of LAB on SRFs

Most SRF studies of the LAB rely on informed but ultimately subjective opinion to decide which negative pulse on the SRF corresponds to the LAB (Fig. S5). In contrast, here we auto-picked the largest-amplitude negative pulse on each SRF in a fixed depth range of 80–220 km, being the shallowest and deepest LAB previously reported in this area from SRF studies (Devi et al., 2011; Hu et al., 2015; Kumar et al., 2006; Liu et al., 2020; Shi et al., 2015; Xu et al., 2021; Xu et al., 2013; Zhao et al., 2011) (Fig. S1). A surface-wave tomographic model (McKenzie et al., 2019) similarly shows the LAB varying from 120–230 km across our study region, supporting our choice to limit the range of depths in which we auto-pick the maximum negative amplitude.

The picked negative S-to-P conversions represent depths of rapidly decreasing wavespeed (NVG) beneath the Moho. The data traces are complex, likely because of violations of our implicit assumption of flat boundaries beneath each 0.5°- or 1.0°-radius bin, and we commonly see multiple negative troughs with similar amplitude on individual traces. Although our automatic method requires a pick of LAB on every trace (Figs. 2, S3, S4) in our interpretations we do not ascribe geological significance to isolated auto-picks (e.g. Fig. 2c, the easternmost pick is 100-km deeper than a nearly equal-amplitude negative trough consistent with all other auto-picks along this profile). Instead, we only interpret areas spanning 200–800 km across which we observe relatively uniform LAB picks (Fig. 4).

A theoretical possibility exists that negative converters immediately below the positive Moho converter represent side-lobes resulting from deconvolution or frequency-filtering

(Kind et al., 2020; Liu et al., 2021; Zhao et al., 2011). Because of the deep Moho (locally ≥80 km) and long-wavelength of S-wave data it is inevitable that the maximum negative amplitude is often the negative peak directly following the Moho positive peak. However, tests of SRF methods without deconvolution or filtering (Kind et al., 2020), analysis of large regional datasets (Liu et al., 2021), and detailed waveform modelling of SRFs in southern Tibet (Zhao et al., 2011) all strongly support the high-amplitude negative converters on stacked SRF data representing real geological boundaries. Scrutiny of the shallow (T-LAB) converter shows lateral variability in waveform character, in delay time after the Moho, and in amplitude relative to the Moho (Fig. 2), making it nearly impossible that T-LAB is only a side-lobe of the Moho pulse. The shallow NVG, where well-imaged as a continuous boundary across multiple traces, should therefore map T-LAB following the consensus of all previous workers in southern Tibet (Devi et al., 2011; Hu et al., 2015; Kumar et al., 2006; Liu et al., 2020; Shi et al., 2015; Xu et al., 2021; Xu et al., 2013; Zhao et al., 2011) and modern reviews of global data (Rychert et al., 2020).

The shallower NVGs (20–50 km below the Moho) are typically more uniform or smoothly varying in depth, so easier to trace (C-C', Fig. 2i) than the deeper converters (D-D', Fig. 2j). Beneath cratons SRFs often image a Mid-Lithospheric Discontinuity (MLD) at depths substantially less than the LAB as inferred from other methods (Liu et al., 2021; Rychert et al., 2020), but no such interpretations have been made in Tibet. It is therefore appropriate to label our deep southern converter as I-LAB while recognizing that the complex and potentially multiple deep NVGs (Figs. S3–S5) may include MLDs within the Indian lithosphere.

2.5. Image resolution

Our image resolution is limited by three effects. [1] Spatial resolution is limited by the 0.5°-radius bins in which we average data, leading to ~50 km uncertainty in placing the lateral boundary between I-LAB and T-LAB. [2] Our SRF images are obtained with the simplest-possible data-processing to minimize bias, and assumes horizontal converters. Hence the termination on our SRF images of a gently dipping converted phase (northern limit of the deep I-LAB converter) could imply the truncation of the converter or could simply indicate the same geologic converter continues but with a steeper dip that defied our imaging. [3] Our auto-picking strategy can only identify one NVG on any one trace, even though it is geologically possible that the shallow and deep boundaries overlap spatially. Hence we derive a likely over-simplified picture of a vertical step in the LAB at the junction of I-LAB and T-LAB. Interpretive extrapolation of the objective (highest-amplitude) picks allows the two LABs to overlap vertically with T-LAB extending south or west a short distance above the northern or eastern limit of I-LAB. For example, on Fig. 2d note a possible prolongation of the shallow NVG further west and of the deeper NVG further east.

3. Results

New SRF and SWS Analyses and Description

We utilize 4,051 SRFs from 462 temporary broadband seismic stations including our 94-station west-east arrays (Shi et al., 2020) that fill data gaps between stations previously deployed along the NNE-trending rift grabens in this region (Kind et al., 2002; Shi et al., 2015; Shi et al., 2016; Zurek, 2008). Our combined dataset has an order-of-magnitude more

data, and correspondingly higher areal resolution, than previous SRF studies in this area. We computed SRFs for all data available to us, even those previously published, to ensure consistent processing (see Methods). We summed the SRFs in uniform 1.0° or 0.5°-radius overlapping circular bins, then auto-picked the maximum negative S-to-P conversion, marking the largest NVG, to provide an objective map of the LAB (Figs. 2, S2). Our mapping shows the highest-amplitude negative converter (blue circles in Figs. 2c-j, S3, S4) is to first order below ~160 km (blue in Fig. 2a,b) in the southwest and above ~130 km (orange and red in Fig. 2a,b) in the northeast of our study area. The transition (hereafter SRF boundary) between the regions of deeper and shallower largest NVGs can be picked sometimes within ±25 km (one-trace spacing) on west-east cross-sections (31°N, Fig. 2d), elsewhere no better than ±100 km (29°N, Fig. 2f) (approximately the degree of data overlap between adjacent bins). The existence and location of this SRF boundary is a key focus of this paper.

Detailed comparison shows that we observe negative-polarity converters at the same depths/locations as seen in older data (Liu et al., 2020) (Fig. S5) even when two studies share no seismic data in common. Likewise, low-frequency SRF traces from sparse older observations confirm the deep NVG at a similar depth to our observations, continuing beneath our whole area (Fig. S6). We conclude that despite different interpretations, SRF images themselves are reliable. Our auto-picked maps (Figs. 2, S2) are noisier than subjectively smoothed maps published elsewhere (Fig. S1), but our first-order, long-wavelength pattern (shallow NVG in southwest, deep NVG in northeast) is seen at different effective resolutions and when bin-centers are offset (Figs. 2a,b, S2). For geologic interpretation we smooth the auto-picks (Fig. 4). Cross-sections ~perpendicular to the SRF

boundary show a step up from a deep southwest converter to a shallow northeast converter (Figs. 2g–j, A-A' and B-B'); whereas sections ~parallel to the boundary show the strongest NVG is everywhere shallow north of the boundary (C-C'), or everywhere deep south of the boundary (D-D').

We used the same 462 broadband stations to derive SWS parameters (split times and fast polarization directions, see 'Methods'), and plot station averages in Fig. 1b, together with published SWS parameters. (For station information, numerical values and contributing publications see Extended Data Tables.) The plotted parameters are the average at each station of the single layer of horizontal transverse anisotropy that best fits each earthquake as recorded at that station.

Just as our SRF data show clear regions with shallow or deep strong NVGs (Fig. 2) so our SWS data (Fig. 3) augment previous results (Chen et al., 2010; Wang et al., 2008) that show clear parameter changes both south to north and west to east across Tibet. Whereas the Tethyan Himalaya and YZS have very variable FPDs where previously well-studied (Chen et al., 2010) southwest of ~30°N, 90°E (Figs. 1b, S7), our new data show that east of ~91°E the Tethyan Himalaya have FPDs aligned consistently across many stations. Spatially consistent FPDs and larger split times are well-known (Chen et al., 2010) from the northern Lhasa and Qiangtang terranes with FPDs sub-parallel to the BNS and JRS even where the sutures turn clockwise to run north-south (Figs. 1b, S7) in a pattern previously correlated with geodetic observations (Wang et al., 2008) . However, when we focus only on FPD azimuth independent of geographic location (Fig. 1b shows FPD deviation from 050°, India absolute plate motion (APM) (Kreemer et al., 2014) we see that the main body of our study area, cutting across all the suture zones, has a rather uniform

NE fast direction (red in Fig. 1b) sandwiched between regions of crudely NW orientations (blue in Fig. 1b). The transition from "NW" to "NE" FPDs in the southwest of our area aligns well with the SRF boundary (Fig. 3).

4. Discussion

4.1. SRF and SWS Interpretation

A positive (red) SRF converter at ~70 km depth (Figs 2c–j, S3, S4) is the Moho as identified in PRF studies (Kind et al., 2002; Nábělek et al., 2009; Shi et al., 2020; Shi et al., 2015). The converter varies between a single high-amplitude peak to a pair of weaker converters (Fig. 2). This pair corresponds to the PRF doublet interpreted as underthrust eclogitized Indian crust at the base of the Tibetan crust (Kind et al., 2002; Nábělek et al., 2009; Shi et al., 2020; Shi et al., 2015) that can reach >25 km, but when <10 km thick merges into a single positive pulse on PRFs (Shi et al., 2020). The transition from SRF doublet to single Moho converter (Fig. 2c-f) marks either an abrupt termination or gradual thinning of underthrust Indian crust, or possibly a transition from a high-velocity eclogitized Indian lower crust (doublet) to a normal mafic (but not eclogite) lower crust lacking a converter at its top.

Our SRF data also allow systematic mapping of the shallower and deeper strongest NVGs (Fig. 2a) with depth modes at ~100–130 km and (much weaker) at ~180–210 km respectively (Fig. S8). We follow previous identifications of the deeper and shallower boundaries as I-LAB and T-LAB (Liu et al., 2020; Shi et al., 2015; Xu et al., 2013; Zhao et al., 2010) (Fig. S1), because Indian lithosphere is Precambrian, cratonic and ~160–200 km thick (Craig et al., 2020; McKenzie et al., 2019) whereas any Tibetan lithosphere

is likely Neogene, younger than the most recent delamination episode beneath Tibet, so much thinner. The greater continuity and clarity of the shallow T-LAB compared to the deeper I-LAB is consistent with global studies comparing Phanerozoic belts (e.g. Tibet) with cratons (e.g. India) (Liu et al., 2021; Rychert et al., 2020). Our images map out the southern limit of T-LAB as the strongest converter, running west-east for >500 km at ~31°N from 88–90°E but north-south along 92°E from ~30–28°N (Figs. 2, 4a). Interpretations of multiple vertically-stacked LABs are precluded by our auto-picking methodology that selects only one NVG per trace (see Methods). Because the Indian plate dips north beneath Tibet (based on tomographic results (Banerjee, 2022; Chen et al., 2017)) we expect I-LAB to extend north and east beyond and below the T-LAB with a degree of horizontal overlap, but in many places to be invisible because of the overlying stronger T-LAB converter. Conversely, a wedge of Tibetan lithosphere that is <~10 km thick so below the resolution limit of our seismograms (Mancinelli et al., 2017) may extend south of the region in which T-LAB is the strongest NVG.

Our SWS data change character close to the SRF boundary. SWS orientations and split times are inherently noisy because they combine signals from asthenosphere, mantle-lithosphere and crust, so interpretations typically use a subjective assessment of broad regional patterns coupled with geographic correlation to infer possible causations. To compare the SRF and SWS results we plot FPDs and split times (Fig. 3) within three 200-km-wide swaths (X, Y, Z in Fig. 1b) across the SRF boundary (Fig. 2). We recognize very scattered FPDs in the southern part of swaths X and Y (to ~50-km north of the YZS) (cyan highlighting in Fig. 3, blue vectors in Fig. 1b), giving way to more consistent NE azimuths further north (pink and red in Figs. 1b, 3) including beyond the BNS. However, along swath

Z we do not see a region of scattered FPDs around the YZS; rather, the NE-oriented FPDs span the YZS and NW-oriented FPDs re-appear northeast of the BNS. The consistent SWS parameters in three geographic zones suggest the anisotropy have distinct geodynamic implications in each of the three zones.

We follow previous studies (Chen et al., 2010; Chen and Özalaybey, 1998) in assuming that the variable FPDs in the southwest portion of our study area represent underthrust Indian lithosphere. Along swaths X and Y these variable or NW-directed FPDs transition northward into northeasterly FPDs, likely a manifestation of the underlying Tibetan lithosphere and/or subjacent asthenosphere. Along swath X there is also a northward jump up in split times, previously suggested to represent the crustal front where the increase was recognized at the same latitude on swath Y (Chen and Özalaybey, 1998). The transition from NW to NE FPDs is ~50 km south of the deep-to-shallow SRF boundary, we suggest due to a thin layer of nascent Tibetan lithosphere influencing the anisotropy but too thin to produce a strong SRF conversion. This region of NE FPDs extends north several hundred kilometers within the area where the shallow T-LAB is the strongest SRF converter. Further east in our study area, where we see FPD rotating clockwise to ~north-south, is the region where the YZS, BNS and JRS rotate from west-east to north-south around the EHS as they transition from a compressional into a strike-slip domain. It has been widely noted that the surface deformation field shows the same clockwise rotation (i.e. modern deformation likely continues to re-orient the sutures into their present position), leading some to conclude that anisotropic structure represents lithospheric deformation (Chang et al., 2015; Wang et al., 2008). These authors (Chang et al., 2015; Wang et al., 2008) rejected the control of FPD by asthenospheric flow because Eurasian

Absolute Plate Motion (APM) is significantly divergent from observed SWS fast directions, though they did not to test the correlation with Indian APM (likely because they only studied stations at the surface of the Eurasian plate, and did not consider whether the region might be underlain by Indian lithosphere). Our newly enlarged database (Fig. 1b) shows an excellent correlation between SWS fast directions and Indian APM both south and north of the YZS, the surficial boundary between Tethyan and Asian terranes. We infer that anisotropy of both nascent Tibetan lithosphere and underlying asthenosphere is controlled by Indian APM.

Our SWS observations on swath Z close to the BNS transition back to NW FPDs (Fig. 1b, 3), perhaps marking the Indian mantle front (Chen et al., 2010). If like previous authors we only had data in the regions of swaths X and Y (Chen et al., 2010), we might conclude that the changes in SWS parameters relate geometrically to the YZS and the BNS that mark the transitions from Tethyan Himalaya to Lhasa to Qiangtang terranes. Swath Z shows that this previously-accepted correlation to sutures and terranes breaks down, and a far better spatial correlation is obtained (Fig. 3) if we align our three swaths along the boundary between deep and shallow strongest negative conversions as mapped out in Fig. 2.

4.2. Interpretations of crustal front, mantle suture and mantle front

The mantle suture is defined as the boundary between Indian mantle and Tibetan or Eurasian mantle at the Moho, and the Indian mantle front as the northernmost extent of the Indian plate (Jin et al., 1996); the crustal front is the northern limit of Indian crust at the Moho. If the northern edge of the Indian plate is vertical from the Moho downwards, then the mantle suture and the crustal and mantle fronts are coincident, and T-LAB and I-LAB

do not overlap. However, if the Indian slab dips north beneath Tibetan lithosphere or an asthenospheric wedge, the mantle suture must be south of the northern limit of I-LAB, and the crustal front could be anywhere at or north of the mantle suture, depending on whether the Indian plate is intact or part or all of the crust is removed during underthrust/subduction (Capitanio et al., 2010). From our SRF data the mantle suture could be at, or is likely some distance south and east of, the southern and eastern limit of where T-LAB forms the largest negative conversion, an uncertainty we represent by showing the SRF mantle suture 100-km-wide in Fig. 4, at 31°N. From our SWS result, the most likely mantle suture location is in the same location, at the transition from NW to NE FPDs (Fig. 1b).

Seismologists largely agree on the position of the crustal front, defined by PRFs at ~31°N from ~83–93°E (Kind et al., 2002; Nábělek et al., 2009; Shi et al., 2015), then possibly turning towards the southeast (Shi et al., 2015); an alternate proxy for the crustal front using H-k analyses of crustal thickness (Wang et al., 2019) shows a very similar southeasterly trend somewhat closer to the EHS (Fig. 4a). West of 90°E the mantle suture appears to be approximately coincident with the crustal front, whether inferred from gravity modelling (Jin et al., 1996), SWS (Chen et al., 2010; Chen and Özalaybey, 1998), the southern limit of geothermal mantle-helium emissions (Hoke et al., 2000; Klemperer et al., 2022), or the northern limit of near-Moho earthquakes (Priestley et al., 2008), all in good agreement with our SRF and SWS data. East of 90°E, where the crustal front remains north of 30°N east to ≥94°E (Kind et al., 2002; Nábělek et al., 2009; Shi et al., 2015; Wang et al., 2019), an SRF image (Shi et al., 2015) and helium-isotope data (Klemperer et al., 2022) have already been used to argue the mantle suture steps >100 km south of the YZS into the

Himalaya, now supported by our interpretations of our SRF boundary and SWS data (Fig. 4a), and by the eastern limit of near-Moho earthquakes (Song and Klemperer, 2023).

Additional supporting evidence for our interpretation of a north-south boundary at ~91–92°E between I-LAB and T-LAB comes from west-east PRF profiles (~29 and 30°N) showing the lower-crust/Moho doublet becomes much thinner (or non-existent) and higher amplitude east of 91–92°E (Shi et al., 2020). The same behavior is seen on our latitudinal SRF profiles (lower frequency than the PRF signals) that show the Moho/doublet converter transitioning from a doublet to a single higher-amplitude pulse at ~91–92°E (Fig. 2c–e). Where Tibetan mantle underlies Indian crust (where the mantle suture is south of the crustal front) Indian lithospheric mantle must be detaching from Indian lower crust. Detachment at the Moho is plausible because the Moho is the weakest intra-lithospheric zone in simple jelly-sandwich strength models, being the deepest/hottest quartz-/feldspar-dominated rocks (Chen and Molnar, 1983). Olivine-dominated mantle at the same depth and temperature is significantly stronger (Chen and Molnar, 1983). The PRF Moho/doublet converters likely bound eclogitized lower crust (Nábělek et al., 2009; Shi et al., 2020). Where the crustal front is north of the mantle suture, new Tibetan lithospheric mantle must be heating underthrust crust. This heated lower crust is too hot for eclogite preservation, explaining the lack of a doublet converter, and too hot for intermediate-depth earthquakes that are indeed absent here (Fig. 4a). Our SRF boundary encompasses all known earthquakes with hypocentral depths 65–100 km (Fig. 4a), that are speculated to mark "India's penetration beneath Tibet or the limit of the Indian Shield as a strong entity" (Priestley et al., 2008), and eclogite drips or Rayleigh-Taylor instabilities (Song and Klemperer, 2023).

Correlations with surface geology and geochemistry are also evident. Our SRF boundary correlates with the northern limit of major normal faulting in Tangra-Yumco graben (TYG), Pumqu-Xainza graben (PXG) and Yadong-Gulu graben (YGG), whereas our eastern margin of Indian lithosphere lies beneath Cona-Sangri graben (CSG), the easternmost of the NNE-trending grabens in southern Tibet (Bian et al., 2020) (Figs. 1a, 4a). This spatial correlation revealed by our map of I-LAB supports a proposed mechanical link between east-west extension and lithospheric underthrusting in southern Tibet (Copley et al., 2011; Wang et al., 2022). These multiple spatial correlations (Fig. 4a) add weight to our identification of our SRF negative converters as observations of distinct I-LAB and T-LAB. Though the correlations are not perfect, discrepancies are within one lithospheric thickness (~100 km), likely representing the potential overlap of the T-LAB/I-LAB boundary as well as imprecision in defining the northern limit of rifts or southern limit of asthenosphere-sourced geothermal ^{3}He. The key aspect of all the datasets is the contrast between the region where Indian crust/mantle together underthrust the Lhasa terrane north of the YZS (A-A', Fig. 4) west of the YGG, and the region where Indian mantle lithosphere delaminates from Indian crust south of the YZS (B-B', Fig. 4) east of the CSG.

4.3. Evolution of Tibetan lithosphere north of the mantle suture

Our geometric model (Fig. 4) is a geologically instantaneous snapshot of lithospheric structure with the mantle suture obliquely crossing the YZS from northwest to southeast. Whether subduction (and the mantle suture) has advanced or retreated with respect to the surface is commonly inferred from migration of magmatism. The interpreted migration of magmatism in eastern Tibet (Kapp and DeCelles, 2019) was southward from ~26–18 Ma, implying slab rollback relative to the upper plate, then northward from ~18–8 Ma

(following an episode of slab break-off) implying slab advance of <~100 km. There are no exposed igneous rocks <8 Ma, so no evidence for the sense or extent of migration since 8 Ma. Neogene high-Mg# ultra-potassic rocks that likely imply mantle melting only occur north of 29°N (Yakovlev et al., 2019) (Fig. 4a) so suggest any slab break-off at ~18 Ma occurred at this latitude (modern co-ordinates) (Craig et al., 2020). The absence of high-Mg# rocks east of 92°E (Fig. 4a) may imply a pre-Neogene boundary in lithospheric structure along or controlling our LAB edge.

Slab break-off at 18 Ma suggests Tibetan mantle lithosphere immediately north of the modern mantle suture at 86–92°E has a thermal age of 18 Ma (or less if underplating Indian lithosphere subsequently extended north of the modern mantle suture). 18-Ma lithosphere is only ~20–50 km thick based on depth to the ~1100°C isotherm (the lowest temperature at which LAB is observed with SRFs in young ocean basins (Rychert and Harmon, 2018)), or depth to the base of the thermal boundary layer, both estimated using conventional thermal parameters (Craig et al., 2020). Despite large uncertainties in these thermal models, T-LAB in southern Tibet should be 20–50 km below the Moho, so at ~70–120 km depth below the surface, in agreement with our observations (Figs. 2, 4b). Even if lithospheric mantle has grown to 50-km thickness by thermal conduction, the 850°C isotherm – the minimum melt temperature at these depths with 0.5% water (Dasgupta, 2018) – is likely reached <5 km below the Moho. Thus a nascent Tibetan lithosphere is a ready source of the ^{3}He anomalies observed everywhere north of the mantle suture (Fig. 4c) whereas the thick underthrust Indian lithosphere is too cold (<600°C at the Moho) (Craig et al., 2020) and too dry (Klemperer et al., 2022) to release ^{3}He.

It is often assumed that slab advance has continued to the present (Craig et al., 2020; Kapp and DeCelles, 2019) despite there being no magmatic record or petrological evidence <8 Ma as to whether hinge advance or hinge retreat is occurring today. The absence of volcanism <8 Ma is not diagnostic of cold Indian underthrusting that prevents magma formation, as the <~15 Ma west-east extension of southern Tibet (Bian et al., 2020) likely traps small-volume partial melts in the mid-crust, for which there is much evidence in southern Tibet (Klemperer, 2006).

East of 92°E far less is known about the timing and polarity of subduction-zone migration. The north-south boundary at 92°E that is the western margin of T-LAB and of high $^3He/^4He$ ratios in thermal springs, and the eastern limit of highly-magnesian igneous rocks younger than 26 Ma, likely marks a west-east change in subduction geometry and lithospheric architecture. This north-south boundary is vertically below the highest-amplitude sub-Moho positive (red) converters (Fig. 2d–f, ~200 km depth below fiducial yellow star) that identify the edge of I-LAB as a zone of complex mantle structure, speculatively even delaminated eclogitized Indian lower crust (Shi et al., 2020). We interpret slab delamination east of 92°E (B-B', Fig. 4c) based on four lines of evidence. [1] The crustal front east of 92°E based on geology (Kapp and DeCelles, 2019), PRFs (Nábělek et al., 2009; Shi et al., 2015; Zhao et al., 2011), and crustal stress state or earthquake focal mechanisms (Copley et al., 2011) (Fig. 1b) is up to 300 km north of the mantle suture, a geometry requiring delamination of Indian mantle lithosphere by detachment from Indian crust. [2] Depths to T-LAB east of the north-south boundary of I-LAB at 92°E [along the possible slab tear inferred from $^3He/^4He$ anomalies (Klemperer et al., 2022)] are ~100 km, consistent with recent roll-back in this region, and even shallower than the ~120-km depth

to T-LAB immediately north of I-LAB from 88–92°E (Figs 2, 4). Hence Tibetan lithosphere is thinner/younger east of 92°E than north of 31°N. [3] SWS directions above T-LAB (Figs 1b, 3) are crudely parallel to Indian APM (~050°) [or India-Eurasia plate convergence direction (~020°), or perpendicular to the boundary between I-LAB and T-LAB], possibly representing asthenospheric flow towards a retreating subduction hinge line (Liu et al., 2019). [4] As elsewhere in Tibet, mantle-sourced ^{3}He in thermal springs (Fig. 4) immediately above the mantle suture requires very young hence hot lithosphere directly beneath the crust (Klemperer et al., 2022), a condition created by slab rollback or delamination. Thus the CSG along 92°E likely marks a tear or abrupt warping of the Indian lithosphere and segmentation of the Himalayan orogen beneath at least the Tethyan Himalaya.

Although numerical modelling suggests tears can be induced just by along-strike variation of convergence rate (Cui and Li, 2022), previous suggestions of slab-tearing beneath the eastern Himalaya and southern Tibet (Bian et al., 2020; Klemperer et al., 2022; Liang et al., 2016; Liu et al., 2020; Ren and Shen, 2008; Shi et al., 2020; Wang et al., 2022; Yin, 2000) commonly presume an association with the NNE-trending Neogene grabens of southern Tibet, most often the largest graben, the YGG (Liang et al., 2016; Wang et al., 2022). But magmatic products of the supposed tear beneath YGG and associated geophysical anomalies span >200 km west-east (Wang et al., 2021; Wang et al., 2022) hence potentially underlying both the YGG and the CSG. Particularly where the crust has been intruded or melted (Wang et al., 2022) mantle extension or upwelling may be laterally displaced from surficial faulting (Tian et al., 2015; Yin, 2000). An analog may be the 'subduction-transform edge propagators' (Govers and Wortel, 2005) that tear the

subducting Adriatic slab and enable its delamination and rollback beneath Italy, and are similarly linked to the surface by broad trans-crustal boundaries that span one-to-two crustal thicknesses perpendicular to the slab tear (Rosenbaum and Piana Agostinetti, 2015).

Oblique convergence between India and Tibet would cause a slab tear to migrate laterally along the west-east orogenic front. We speculate that the lithospheric edge or tear seen today beneath the CSG (Klemperer et al., 2022; Ren and Shen, 2008; Shi et al., 2020) (Figs 1b, 4) may have been associated with mid-Miocene magmatism centered on the YGG, but today is localized further east beneath the CSG where mid-Miocene diffuse extension only gave way to focused rifting at ~3 Ma (Bian et al., 2020). The CSG overlies a significant lateral ramp in the Main Himalayan Thrust, along a north-south fault (Cona cross-structure) that can be traced south into the High Himalaya (Wei et al., 2022), potentially linking to the orogen-crossing Kopili fault zone (Fig. 1a) that has hosted a historic M_W ~7 earthquake within the Indian basement (Bilham, 2019). Himalayan seismic hazard is controlled by along-strike segmentation of the thrust belt into distinct earthquake rupture zones. A prominent seismic gap from 91–94°E that has slip deficit ≥11 m and is at risk of a M_W ≥8.7 earthquake may be bounded to the west by the Kopili fault zone (Bilham, 2019). An association between our observed slab tear, the Cona-Sangri graben in the upper (Tibetan) thrust plate and the Kopili strike-slip fault in the lower (Indian) plate would suggest that segmentation of the seismogenic upper crust has its origins at the deepest orogenic level, in the mantle lithosphere.

5. Conclusion

Our SRFs objectively map depths to distinct Indian and Tibetan lithosphere-asthenosphere boundaries across a substantial region of south-eastern Tibet

(~500×1000 km). The inferred boundary between the two lithospheres is corroborated by more subjective mapping of changing SWS parameters, and by independent interpretations of the mantle suture from mantle degassing patterns and the northern limit of sub-Moho earthquakes. The southern limit of Tibetan lithosphere and subjacent asthenosphere is at 31°N west of 90°E but steps south by >300 km to ~28°N east of 92°E likely representing a slab tear. Displacement of the mantle suture 300 km south of the crustal front and Tibetan mantle-lithosphere thickness <30 km suggest geologically recent, likely ongoing, slab rollback and delamination east of 92°E. Slab rollback and fragmentation from the CSG east to the EHS may be the structural consequence of the geometric difficulty of simultaneously subducting Indian lithosphere northward beneath Tibet and eastward beneath the active Burma volcanic arc (Li et al., 2008; Zheng et al., 2020).

Author contributions

D.S. designed and carried out the fieldwork and computed the SRFs; L.L. analyzed the data and prepared visualizations and maps; S.L.K. led the tectonic analysis; J.S. calculated the shear-wave splitting parameters; S.L.K., L.L. and D.S. wrote the paper.

Competing interests

All the authors declare that they have no competing interests.

Data and materials availability

We have made available the following data: (1) Locations and operating periods of all stations from which data were analyzed in this study; (2) All 4,051 SRFs with piercing points shown in Fig. 1a, calculated according to the 'Data and Methods'; (3) Individual SWS results for all events analyzed at all stations, and station averages plotted in Figs. 1b and S7.

Figures
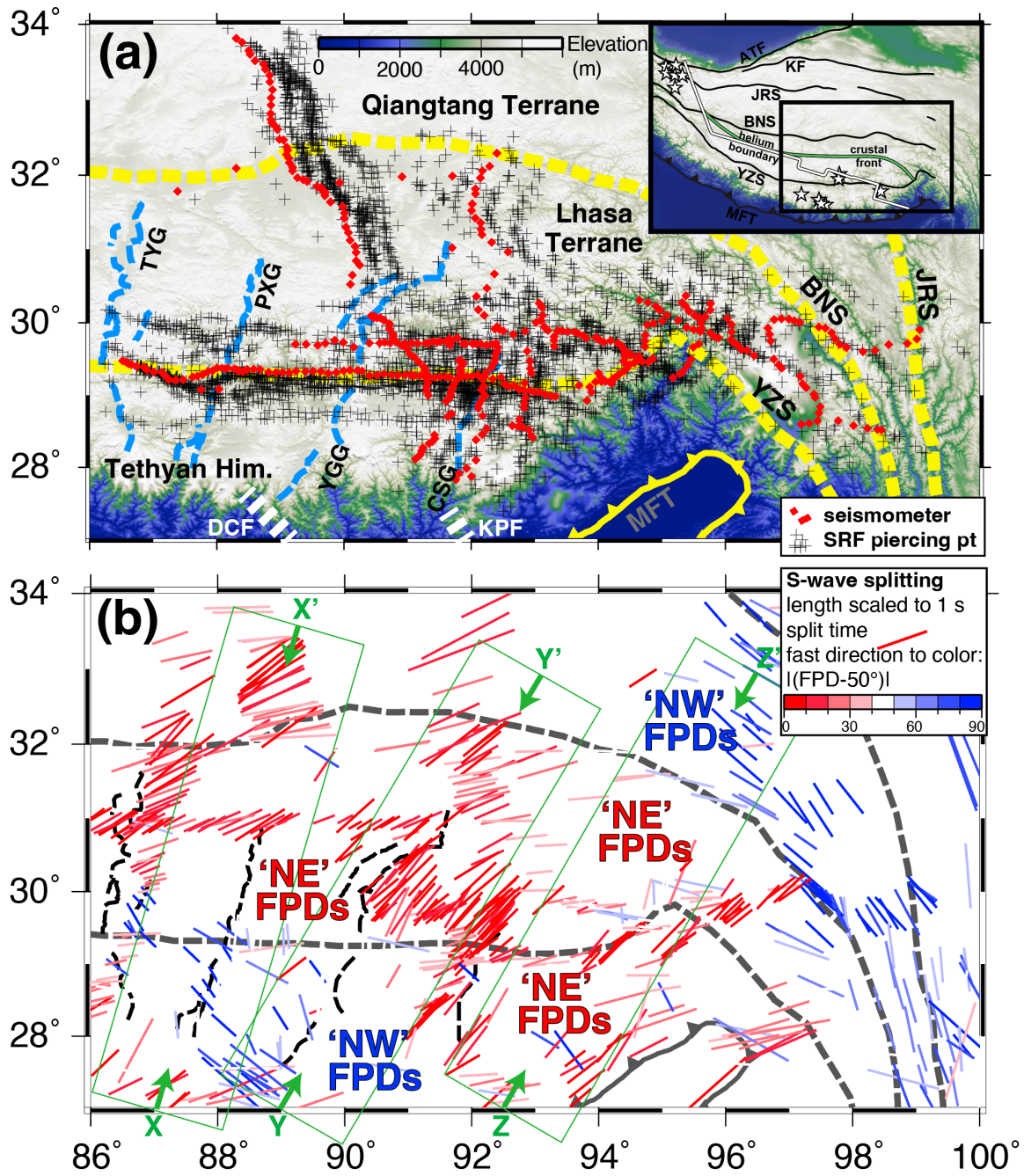
Fig. 1. (a) Shaded-relief map of southern Tibet showing seismometers (red diamonds) and SRF piercing points at 150 km (black crosses). Yellow dash lines: Yarlung-Zangbo (YZS), Banggong-Nujiang (BNS) and Jinsha River (JRS) sutures; and Main Frontal Thrust (MFT).

Blue dash lines: normal faults in the Tangra-Yumco (TYG), Pumqu-Xainza (PXG), Yadong-Gulu (YGG), and Cona-Sangri (CSG) grabens (Taylor and Yin, 2009). Orogen-crossing earthquake alignments: Dhubri-Chungthang fault zone (DCF), Kopili fault zone (KPF) (Dal Zilio et al., 2021). Inset map shows Indian crustal front, helium boundary (mantle suture) and below-Moho earthquakes (stars) (Klemperer et al., 2022); Kunlun fault (KF); Altyn Tagh fault (ATF). (b) Shear-wave splitting results, this study and (Chen and Özalaybey, 1998): fast polarization directions (FPDs) colored with respect to Indian absolute plate motion, 050° and length scaled to split time. Green arrows and 200-km wide boxes are transects X, Y and Z shown in Fig. 3.

Fig. 2. Maps of depth to auto-picked largest negative velocity gradient (NVG) on SRFs stacked in (a) 1° and (b) 0.5° radius bins. Color scale indicates depth to NVG and opacity is proportional to the number of SRFs per bin (fully transparent if < 3 SRFs in a bin; numbers of SRFs shown in Fig. S2). Stars mark locations of SRF boundary (transition from deep (blue) to shallow (red) strongest NVG) identified on latitudinal profiles (yellow stars) and on oblique profiles AA' and BB' (white stars). (c)–(f) Record sections in 1° radius bins plotted along latitudinal profiles 32°, 31°, 30° and 29°N as shown in (a). (g)–(j) Record sections in 0.5° radius bins plotted along oblique profiles AA', BB', CC' and DD' as in (b). Blue circles are auto-picked maximum negative arrivals between 80 and 220 km, as mapped in (a) and (b). Pale cyan and pink bars beneath record sections show regions of strongest deep and shallow NVGs, also interpreted as I-LAB and T-LAB. White triangles (c, d, e, f) mark doublet and Moho peaks, shown only where two peaks appear in the range 50–90 km (shallowest and deepest PRF converters in Shi et al. (2020)). All record sections are vertically exaggerated x2 and have the same horizontal scale as the maps.
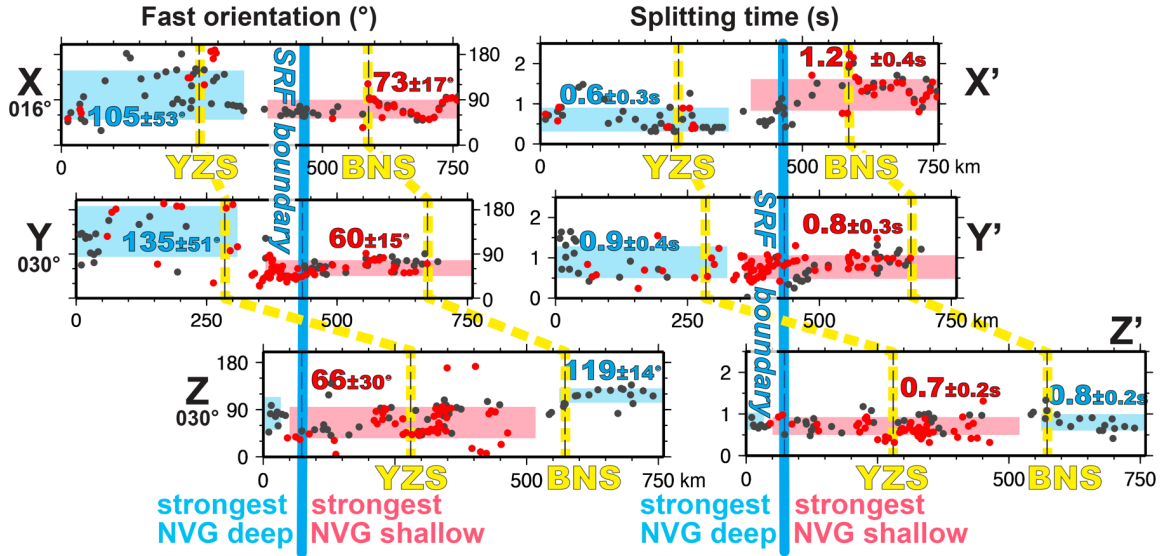
Fig. 3. SWS fast directions and split times for transects XX', YY' and ZZ' (Fig. 1b) oriented ~orthogonal to the boundary between I-LAB and T-LAB inferred from SRFs (Fig. 2). Red dots are new measurements; black dots are literature values. The three transects are aligned along the LAB boundary (vertical cyan line), and yellow dog-leg dashed lines link locations of YZS and BNS on the three transects. Pink shading from ~50 km south to >300 km north of I-LAB/T-LAB boundary shows region of NE FPDs and uniform split times; cyan shading marks regions of more scattered or SE FPDs across YZS (X-X' and Y-Y'); averages and standard deviations are shown for each shaded group. Boundary between groups is subjective, but aligns far better with SRF boundary than with suture zones.
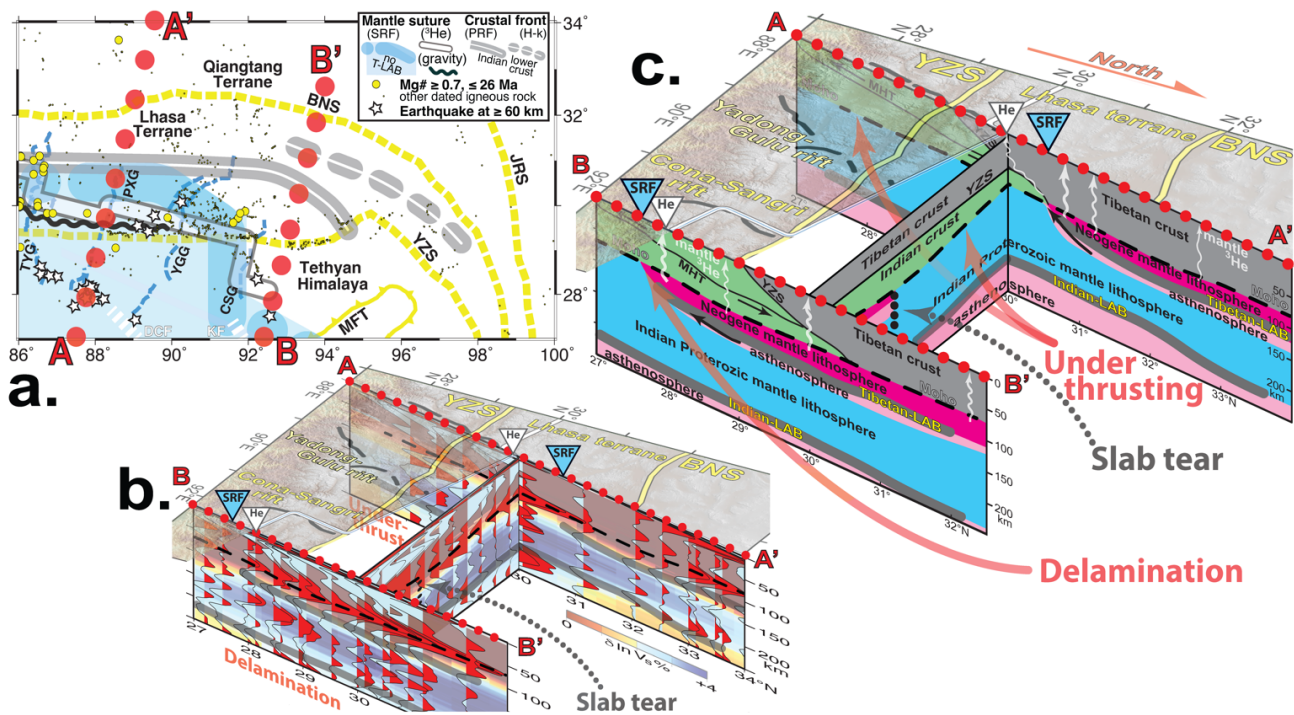
Fig. 4. (a) Summary of SRF and SWS results and location of cross-sections A-A' and B-B' in b and c. Southwestern region (pale cyan) has no Tibetan mantle lithosphere; thick cyan boundary is shown 100-km wide to capture uncertainty in location of SRF mantle suture. Smoothly curved thin white line with thick grey margins is northern extent of Indian lower crust at the Moho (crustal front), continuous line from PRF doublet (Kind et al., 2002; Nábělek et al., 2009; Shi et al., 2015), dashed line from H-k Moho mapping (Wang et al., 2019). Dog-legged thick white line with thick grey margins is helium boundary line interpreted as mantle suture (Klemperer et al., 2022). White stars are earthquakes with hypocenters at 65–100 km depth (Klemperer et al., 2022). Yellow circles: igneous rocks (Yakovlev et al., 2019) with Mg# ≥0.7 and age ≤26 Ma; tiny yellow dots: all other dated igneous rocks. (b) 3D perspective of SE Tibet viewed from the northeast, showing interpretation of Moho (dashed line), I-LAB and T-LAB (broad grey lines) superimposed on three SRF sections (no vertical exaggeration), AA' and BB' parallel to India-
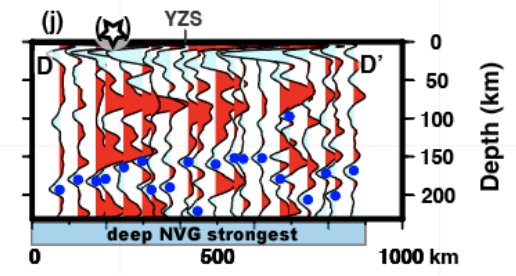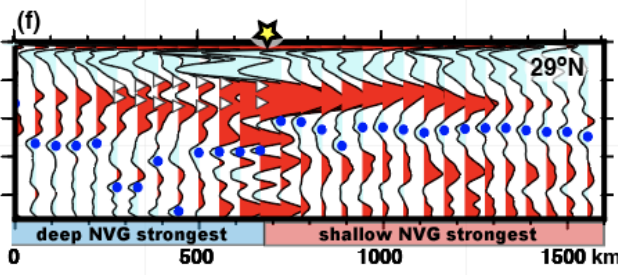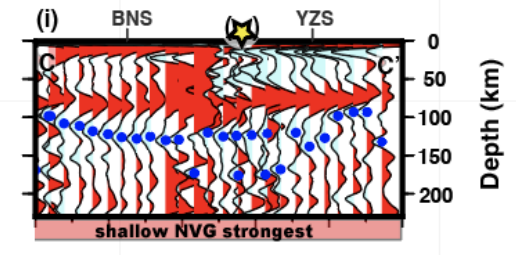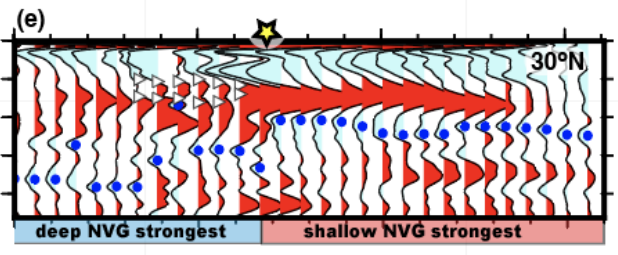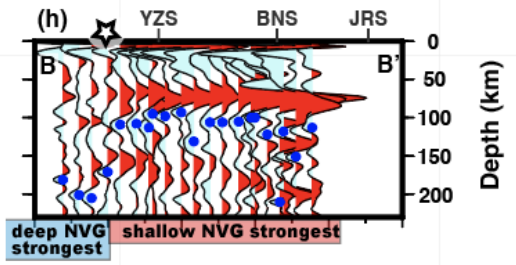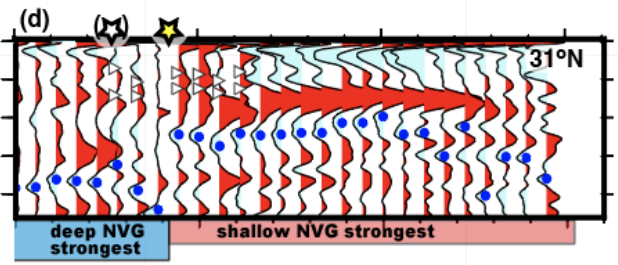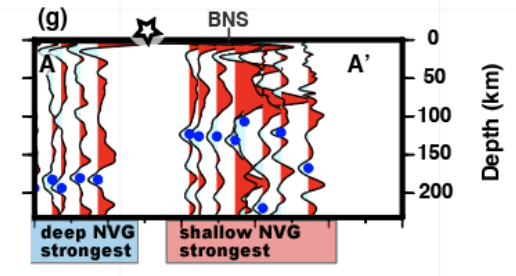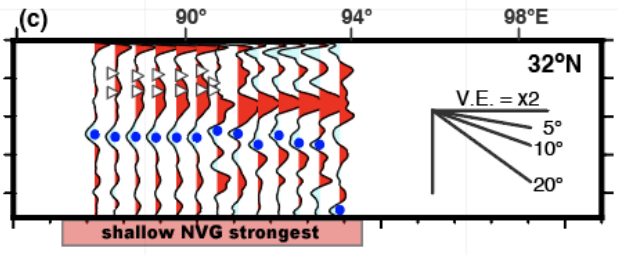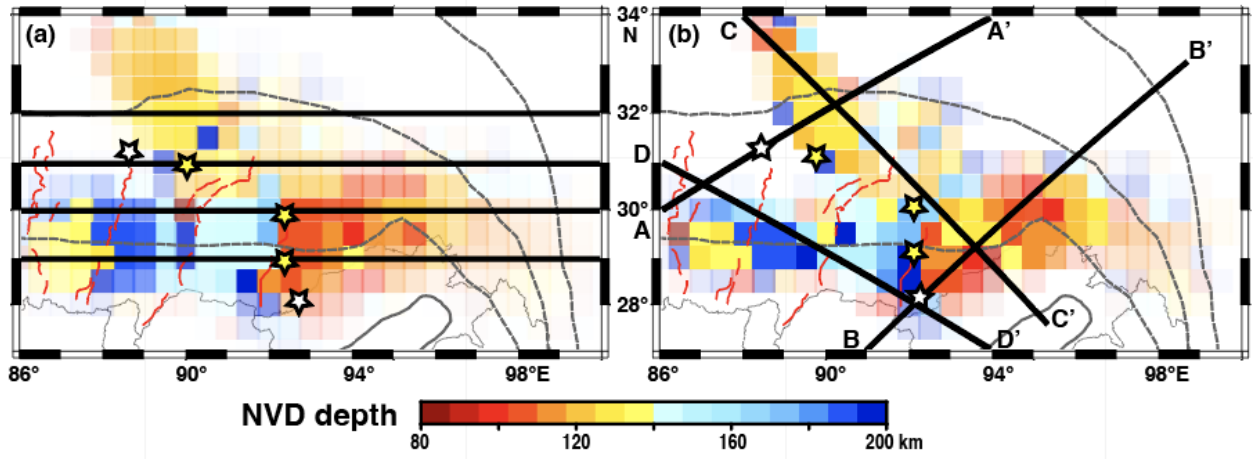
40 convergence direction (cf. Fig. 2) and 30°N (Fig. S6) and on seismic tomography model

41 (Chen et al., 2017) plotted as % dlnVs (see Fig. S6) (blue: higher wavespeed than average

42 at 150-km depth, inferred cratonic mantle lithosphere; red: slow wavespeeds below Moho,

43 inferred Neogene mantle lithosphere). Transparent shaded-relief map shows yellow lines:

44 YZS and BNS sutures; black lines: normal faults in the active rifts PXG, YGG and CSG;

45 white line: helium boundary, all as in a. Blue and white triangles mark mantle suture

46 interpreted from SRF (this paper) and ^{3}He/^{4}He measurements (Klemperer et al., 2022). (c)

47 3D perspective view of cartoon cross-sections at true-scale (no vertical exaggeration) along

48 AA', BB' and 30°N. I-LAB and T-LAB re-drawn from (b); Moho, YZS and MHT are from

49 PRF studies (Kind et al., 2002; Nábělek et al., 2009; Shi et al., 2020; Shi et al., 2015).

50 Wiggly lines are schematic of ^{3}He leaking from hot Neogene mantle lithosphere or

51 subjacent asthenosphere everywhere north of the mantle suture.

52

53

54

55

56

57

58

59

60

61

References

Ammon, C.J., 1991. The isolation of receiver effects from teleseismic P waveforms. Bull. Seismol. Soc. Am. 81, 2504-2510.

Banerjee, R., Liu, C., Grand, S., Mitra, S., Sandvol, E.A. and Liang, X., 2022. Extent and Evolution of the Indian Cratonic Lithosphere (ICL) Determined by Full Waveform Inversion Tomography. In AGU Fall Meeting Abstracts.

Barazangi, M., Ni, J., 1982. Velocities and propagation characteristics of Pn and Sn beneath the Himalayan arc and Tibetan plateau: Possible evidence for underthrusting of Indian continental lithosphere beneath Tibet. Geology 10, 179-185.

Bian, S., Gong, J., Zuza, A.V., Yang, R., Tian, Y., Ji, J., Chen, H., Xu, Q., Chen, L., Lin, X., Cheng, X., Tu, J., Yu, X., 2020. Late Pliocene onset of the Cona rift, eastern Himalaya, confirms eastward propagation of extension in Himalayan-Tibetan orogen. Earth and Planetary Science Letters 544, 116383.

Bilham, R., 2019. Himalayan earthquakes: a review of historical seismicity and early 21st century slip potential. Geological Society, London, Special Publications 483, 423-482.

Capitanio, F.A., Morra, G., Goes, S., Weinberg, R.F., Moresi, L., 2010. India-Asia convergence driven by the subduction of the Greater Indian continent. Nature Geoscience 3, 136-139.

Chang, L., Flesch, L.M., Wang, C.-Y., Ding, Z., 2015. Vertical coherence of deformation in lithosphere in the eastern Himalayan syntaxis using GPS, Quaternary fault slip rates, and shear wave splitting data. Geophysical Research Letters 42, 5813-5819.

Chen, M., Niu, F., Tromp, J., Lenardic, A., Lee, C.A., Cao, W., Ribeiro, J., 2017. Lithospheric foundering and underthrusting imaged beneath Tibet. Nature Communications 8, 15659.

Chen, W.-P., Martin, M., Tseng, T.-L., Nowack, R.L., Hung, S.-H., Huang, B.-S., 2010. Shear-wave birefringence and current configuration of converging lithosphere under Tibet. Earth and Planetary Science Letters 295, 297-304.

Chen, W.-P., Molnar, P., 1983. Focal depths of intracontinental and intraplate earthquakes and their implications for the thermal and mechanical properties of the lithosphere. Journal of Geophysical Research: Solid Earth 88, 4183-4214.

Chen, W.-P., Özalaybey, S., 1998. Correlation between seismic anisotropy and Bouguer gravity anomalies in Tibet and its implications for lithospheric structures. Geophysical Journal International 135, 93-101.

Copley, A., Avouac, J.-P., Wernicke, B.P., 2011. Evidence for mechanical coupling and strong Indian lower crust beneath southern Tibet. Nature 472, 79-81.

Craig, T.J., Kelemen, P.B., Hacker, B.R., Copley, A., 2020. Reconciling Geophysical and Petrological Estimates of the Thermal Structure of Southern Tibet. Geochemistry, Geophysics, Geosystems 21, e2019GC008837.

Cui, Q., Li, Z.-H., 2022. Along-Strike Variation of Convergence Rate and Pre-Existing Weakness Contribute to Indian Slab Tearing Beneath Tibetan Plateau. Geophysical Research Letters 49, e2022GL098019.

Dal Zilio, L., Hetényi, G., Hubbard, J., Bollinger, L., 2021. Building the Himalaya from tectonic to earthquake scales. Nature Reviews Earth & Environment 2, 251-268.

Dasgupta, R., 2018. Volatile-bearing partial melts beneath oceans and continents–Where, how much, and of what compositions? American Journal of Science 318, 141.

Devi, E.U., Kumar, P., Kumar, M.R., 2011. Imaging the Indian lithosphere beneath the Eastern Himalayan region. Geophysical Journal International 187, 631-641.

Dueker, K.G., Sheehan, A.F., 1997. Mantle discontinuity structure from midpoint stacks of converted P to S waves across the Yellowstone hotspot track. Journal of Geophysical Research: Solid Earth 102, 8313-8327.

112   Faber, S., Müller, G., 1980. Sp phases from the transition zone between the upper and
113   lower mantle. Bulletin of the Seismological Society of America 70, 487-508.

114   Govers, R., Wortel, M.J.R., 2005. Lithosphere tearing at STEP faults: response to edges
115   of subduction zones. Earth and Planetary Science Letters 236, 505-523.

116   Hoke, L., Lamb, S., Hilton, D.R., Poreda, R.J., 2000. Southern limit of mantle-derived
117   geothermal helium emissions in Tibet: implications for lithospheric structure. Earth and
118   Planetary Science Letters 180, 297-308.

119   Hu, J., Yang, H., Li, G., Peng, H., 2015. Seismic upper mantle discontinuities beneath
120   Southeast Tibet and geodynamic implications. Gondwana Research 28, 1032-1047.

121   Jin, Y., McNutt, M.K., Zhu, Y.-s., 1996. Mapping the descent of Indian and Eurasian
122   plates beneath the Tibetan Plateau from gravity anomalies. Journal of Geophysical
123   Research: Solid Earth 101, 11275-11290.

124   Kapp, P., DeCelles, P.G., 2019. Mesozoic–Cenozoic geological evolution of the
125   Himalayan-Tibetan orogen and working tectonic hypotheses. American Journal of
126   Science 319, 159.

127   Kind, R., Mooney, W.D., Yuan, X., 2020. New insights into structural elements of the
128   upper mantle beneath the contiguous United States from S-to-P converted seismic waves.
129   Geophysical Journal International 222, 646-659.

130   Kind, R., Yuan, X., Kumar, P., 2012. Seismic receiver functions and the lithosphere–
131   asthenosphere boundary. Tectonophysics 536-537, 25-43.

132   Kind, R., Yuan, X., Saul, J., Nelson, D., Sobolev, S.V., Mechie, J., Zhao, W., Kosarev,
133   G., Ni, J., Achauer, U., Jiang, M., 2002. Seismic images of crust and upper mantle
134   beneath Tibet: evidence for Eurasian plate subduction. Science 298, 1219-1221.

135   Klemperer, S.L., 2006. Crustal flow in Tibet: geophysical evidence for the physical state
136   of Tibetan lithosphere, and inferred patterns of active flow. Geol. Soc., London, Spec.
137   Publ. 268, 39-70.

138 Klemperer, S.L., Zhao, P., Whyte, C.J., Darrah, T.H., Crossey, L.J., Karlstrom, K.E., Liu,
139 T., Winn, C., Hilton, D.R., Ding, L., 2022. Limited underthrusting of India below Tibet:
140 3He/4He analysis of thermal springs locates the mantle suture in continental collision.
141 Proc. Natl. Acad. Sci. U.S.A. 119, e2113877119.

142 Kreemer, C., Blewitt, G., Klein, E.C., 2014. A geodetic plate motion and Global Strain
143 Rate Model. Geochemistry, Geophysics, Geosystems 15, 3849-3889.

144 Kumar, P., Yuan, X., Kind, R., Ni, J., 2006. Imaging the colliding Indian and Asian
145 Lithospheric plates beneath Tibet. Journal of Geophysical Research: Atmospheres 111.

146 Li, C., van der Hilst, R.D., Meltzer, A.S., Engdahl, E.R., 2008. Subduction of the Indian
147 lithosphere beneath the Tibetan Plateau and Burma. Earth and Planetary Science Letters
148 274, 157-168.

149 Liang, X., Chen, Y., Tian, X., Chen, Y.J., Ni, J., Gallegos, A., Klemperer, S.L., Wang,
150 M., Xu, T., Sun, C., Si, S., Lan, H., Teng, J., 2016. 3D imaging of subducting and
151 fragmenting Indian continental lithosphere beneath southern and central Tibet using
152 body-wave finite-frequency tomography. Earth and Planetary Science Letters 443, 162-
153 175.

154 Liu, L., Gao, S.S., 2018. Lithospheric layering beneath the contiguous United States
155 constrained by S-to-P receiver functions. Earth and Planetary Science Letters 495, 79-86.

156 Liu, L., Gao, S.S., Liu, K.H., Li, S., Tong, S., Kong, F., 2019. Toroidal Mantle Flow
157 Induced by Slab Subduction and Rollback Beneath the Eastern Himalayan Syntaxis and
158 Adjacent Areas. Geophysical Research Letters 46, 11080-11090.

159 Liu, L., Klemperer, S., Blanchette, A., 2021. Western Gondwana imaged by S receiver-
160 functions (SRF): new results on Moho, MLD (mid-lithospheric discontinuity) and LAB
161 (lithosphere-asthenosphere boundary). Gondwana Research 96, 206-218.

162 Liu, Z., Tian, X., Yuan, X., Liang, X., Chen, Y., Zhu, G., Zhang, H., Li, W., Tan, P., Zuo,
163 S., Wu, C., Nie, S., Wang, G., Yu, G., Zhou, B., 2020. Complex structure of upper mantle

164 beneath the Yadong-Gulu rift in Tibet revealed by S-to-P converted waves. Earth and

165 Planetary Science Letters 531, 115954.

166 Long, M.D., Silver, P.G., 2009. Shear Wave Splitting and Mantle Anisotropy:

167 Measurements, Interpretations, and New Directions. Surveys in Geophysics 30, 407-461.

168 Mancinelli, N.J., Fischer, K.M., Dalton, C.A., 2017. How Sharp Is the Cratonic

169 Lithosphere-Asthenosphere Transition? Geophysical Research Letters 44, 10,189-

170 110,197.

171 McKenzie, D.P., Jackson, J., Priestley, K.F., 2019. Continental collisions and the origin

172 of subcrustal continental earthquakes. Canadian Journal of Earth Sciences.

173 Nábělek, J., Hetenyi, G., Vergne, J., Sapkota, S., Kafle, B., Jiang, M., Su, H., Chen, J.,

174 Huang, B.S., Team, H.C., 2009. Underplating in the Himalaya-Tibet Collision Zone

175 Revealed by the Hi-CLIMB Experiment. Science 325, 1371-1374.

176 Nunn, C., Roecker, S.W., Priestley, K.F., Liang, X., Gilligan, A., 2014. Joint inversion of

177 surface waves and teleseismic body waves across the Tibetan collision zone: the fate of

178 subducted Indian lithosphere. Geophysical Journal International 198, 1526-1542.

179 Priestley, K., Jackson, J., McKenzie, D., 2008. Lithospheric structure and deep

180 earthquakes beneath India, the Himalaya and southern Tibet. Geophysical Journal

181 International 172, 345-362.

182 Ren, Y., Shen, Y., 2008. Finite frequency tomography in southeastern Tibet: Evidence

183 for the causal relationship between mantle lithosphere delamination and the north–south

184 trending rifts. Journal of Geophysical Research: Solid Earth 113.

185 Rosenbaum, G., Piana Agostinetti, N., 2015. Crustal and upper mantle responses to

186 lithospheric segmentation in the northern Apennines. Tectonics 34, 648-661.

187 Rychert, C.A., Harmon, N., 2018. Predictions and Observations for the Oceanic

188 Lithosphere From S-to-P Receiver Functions and SS Precursors. Geophysical Research

189 Letters 45, 5398-5406.

190   Rychert, C.A., Harmon, N., Constable, S., Wang, S., 2020. The Nature of the
191   Lithosphere-Asthenosphere Boundary. Journal of Geophysical Research: Solid Earth 125,
192   e2018JB016463.

193   Savage, M.K., 1999. Seismic anisotropy and mantle deformation: What have we learned
194   from shear wave splitting? Reviews of Geophysics 37, 65-106.

195   Shi, D., Klemperer, S.L., Shi, J., Wu, Z., Zhao, W., 2020. Localized foundering of Indian
196   lower crust in the India-Tibet collision zone. Proceedings of the National Academy of
197   Sciences of the United States of America 117, 24742-24747.

198   Shi, D., Wu, Z., Klemperer, S.L., Zhao, W., Xue, G., Su, H., 2015. Receiver function
199   imaging of crustal suture, steep subduction, and mantle wedge in the eastern India–Tibet
200   continental collision zone. Earth and Planetary Science Letters 414, 6-15.

201   Shi, D., Zhao, W., Klemperer, S.L., Wu, Z., Mechie, J., Shi, J., Xue, G., Su, H., 2016.
202   West–east transition from underplating to steep subduction in the India–Tibet collision
203   zone revealed by receiver-function profiles. Earth and Planetary Science Letters 452,
204   171-177.

205   Silver, P.G., Chan, W.W., 1991. Shear wave splitting and subcontinental mantle
206   deformation. Journal of Geophysical Research: Solid Earth 96, 16429-16454.

207   Song, X., Klemperer, S., 2023. Numerous Tibetan lower-crustal and upper-mantle
208   earthquakes detected by Sn/Lg ratios suggest crustal delamination or drip tectonics.

209   Taylor, M., Yin, A., 2009. Active structures of the Himalayan-Tibetan orogen and their
210   relationships to earthquake distribution, contemporary strain field, and Cenozoic
211   volcanism. Geosphere 5, 199-214.

212   Tian, X., Yun, C., Tseng, T.L., Klemperer, S.L., Teng, J., 2015. Weakly coupled
213   lithospheric extension in southern Tibet. Earth and Planetary Science Letters 430, 171-
214   177.

215   Wang, C.-Y., Flesch, L.M., Silver, P.G., Chang, L.-J., Chan, W.W., 2008. Evidence for
216   mechanically coupled lithosphere in central Asia and resulting implications. Geology 36.

217   Wang, C.Y., Mooney, W.D., Zhu, L., Wang, X., Lou, H., You, H., Cao, Z., Chang, L.,
218   Yao, Z., 2019. Deep Structure of the Eastern Himalayan Collision Zone: Evidence for
219   Underthrusting and Delamination in the Postcollisional Stage. Tectonics 38, 3614-3628.

220   Wang, R., Weinberg, R.F., Zhu, D.-C., Hou, Z.-Q., Yang, Z.-M., 2021. The impact of a
221   tear in the subducted Indian plate on the Miocene geology of the Himalayan-Tibetan
222   orogen. GSA Bulletin 134, 681-690.

223   Wang, S., Replumaz, A., Chevalier, M.-L., Li, H., 2022. Decoupling between upper
224   crustal deformation of southern Tibet and underthrusting of Indian lithosphere. Terra
225   Nova 34, 62-71.

226   Wei, J., Wang, A., Lyu, G., Liu, Y., Li, H., Shen, T., Wang, G., 2022. Tectonic
227   segmentation by N-S-trending cona cross structure in the Eastern Himalaya: Evidence
228   from thermochronology and thermokinematic modeling. Tectonophysics 839, 229527.

229   Xu, Q., Liu, H., Yuan, X., Zhao, J., Pei, S., 2021. Eastward Dipping Style of the
230   Underthrusting Indian Lithosphere Beneath the Tethyan Himalaya Illuminated by P and S
231   Receiver Functions. Journal of Geophysical Research: Solid Earth 126, e2020JB021219.

232   Xu, Q., Zhao, J., Pei, S., Liu, H., 2013. Imaging lithospheric structure of the eastern
233   Himalayan syntaxis: New insights from receiver function analysis. Journal of
234   Geophysical Research: Solid Earth 118, 2323-2332.

235   Yakovlev, P.V., Saal, A., Clark, M.K., Hong, C., Mallick, S., 2019. The geochemistry of
236   Tibetan lavas: Spatial and temporal relationships, tectonic links and geodynamic
237   implications. Earth and Planetary Science Letters 520, 115-126.

238   Yin, A., 2000. Mode of Cenozoic east-west extension in Tibet suggesting a common
239   origin of rifts in Asia during the Indo-Asian collision. Journal of Geophysical Research:
240   Solid Earth.

241   Zhao, J., Yuan, X., Liu, H., Kumar, P., Pei, S., Kind, R., Zhang, Z., Teng, J., Ding, L.,

242   Gao, X., Xu, Q., Wang, W., 2010. The boundary between the Indian and Asian tectonic

243   plates below Tibet. Proceedings of the National Academy of Sciences of the United

244   States of America 107, 11229-11233.

245   Zhao, W., Kumar, P., Mechie, J., Kind, R., Meissner, R., Wu, Z., Shi, D., Su, H., Xue, G.,

246   Karplus, M., 2011. Tibetan plate overriding the Asian plate in central and northern Tibet.

247   Nature Geoscience 4, 870-873.

248   Zheng, T., He, Y., Ding, L., Jiang, M., Ai, Y., Mon, C.T., Hou, G., Sein, K., Thant, M.,

249   2020. Direct structural evidence of Indian continental subduction beneath Myanmar.

250   Nature Communications 11, 1944.

251   Zurek, B., 2008. The evolution and modification of continental lithosphere, dynamics of

252   'indentor corners' and imaging the lithosphere across the eastern syntaxis of Tibet. Ph.D.

253   thesis, Lehigh University, Bethlehem, PA 259.

254

Supplementary Materials

Slab tearing and delamination of the Indian lithospheric mantle during flat-slab subduction, southeast Tibet

Lin LIU[a, 1], Danian SHI[b], Simon L. KLEMPERER[c, 1], Jianyu SHI[d]

[a]Frontiers Science Center for Deep Ocean Multispheres and Earth System, Key Lab of Submarine Geosciences and Prospecting Techniques, MOE and College of Marine Geosciences, Ocean University of China, 266100 Qingdao, China;
[b]Chinese Academy of Geological Sciences, 100037 Beijing, China;
[c]Department of Geophysics, Stanford University, Stanford, CA 94305-2215;
[d]National Marine Environmental Forecasting Center, Beijing 100081, China

Figures S1-S10

Tables S1-S2

Table S1a. Mean splitting parameters per station obtained from all previous shear-wave splitting publications.

Table S1b. Null measurements obtained from all previous shear-wave splitting publications.

Table S2a. All individual shear-wave splitting parameters obtained from new seismic stations in our study area.

Table S2b. Mean splitting parameters per station calculated from new seismic stations in our study area.

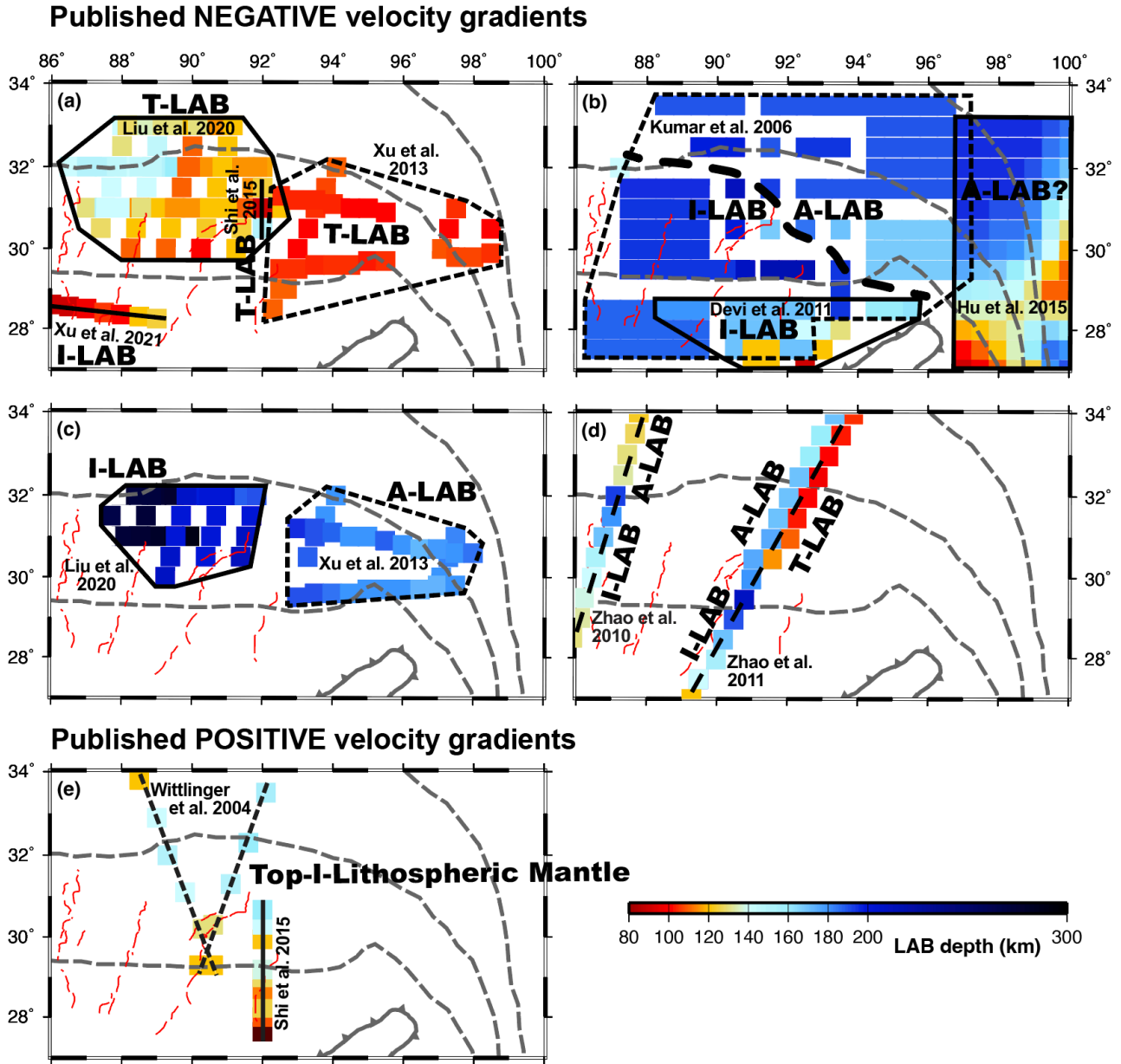*Table S2c. Null measurements obtained from new seismic stations in our study area.*

Fig. S1. (a-d) LAB depth (*negative* wavespeed gradient with depth) interpreted by previous SRF studies as Indian or Tibetan or Asian LAB (I-LAB or T-LAB or A-LAB). (a) Studies reporting LAB depths mostly <130 km. (b, c) Studies reporting LAB depths mostly >170 km; studies in (c) are the same as in (a). (d) Studies identifying multiple LABs on a single profile. Note conflicting results: in some locations picks differ by >50 km vertically in the same location, e.g. in the west-center of our study area compare interpretations of I-LAB at ~250 km (part c), ~200 km (part b), and ~150 km (part d). Note conflicting interpretations of the same converter, e.g. A-LAB (part c) spans both A-LAB and I-LAB (Part b); and the same interpretation of different converters, e.g. I-

LAB (part a) cannot be the I-LAB (part b) because their depths differ by >100 km. Faults and suture zones as in Fig. 1a; area of figure matches Fig. 1. Contributing studies shown here are Devi et al. (2011), Hu et al. (2015), Kumar et al. (2006), Liu et al. (2020), Shi et al. (2015), Xu et al. (2013; 2021), Zhao et al. (2010; 2011). **(e) Depths to top of subducting Indian lithospheric mantle (*positive* wavespeed gradient with depth)** interpreted by previous SRF studies, plotted with the same color-bar and all other symbols as Fig. S1a-d. Contributing studies shown here are Wittlinger et al. (2004) and Shi et al. (2015).
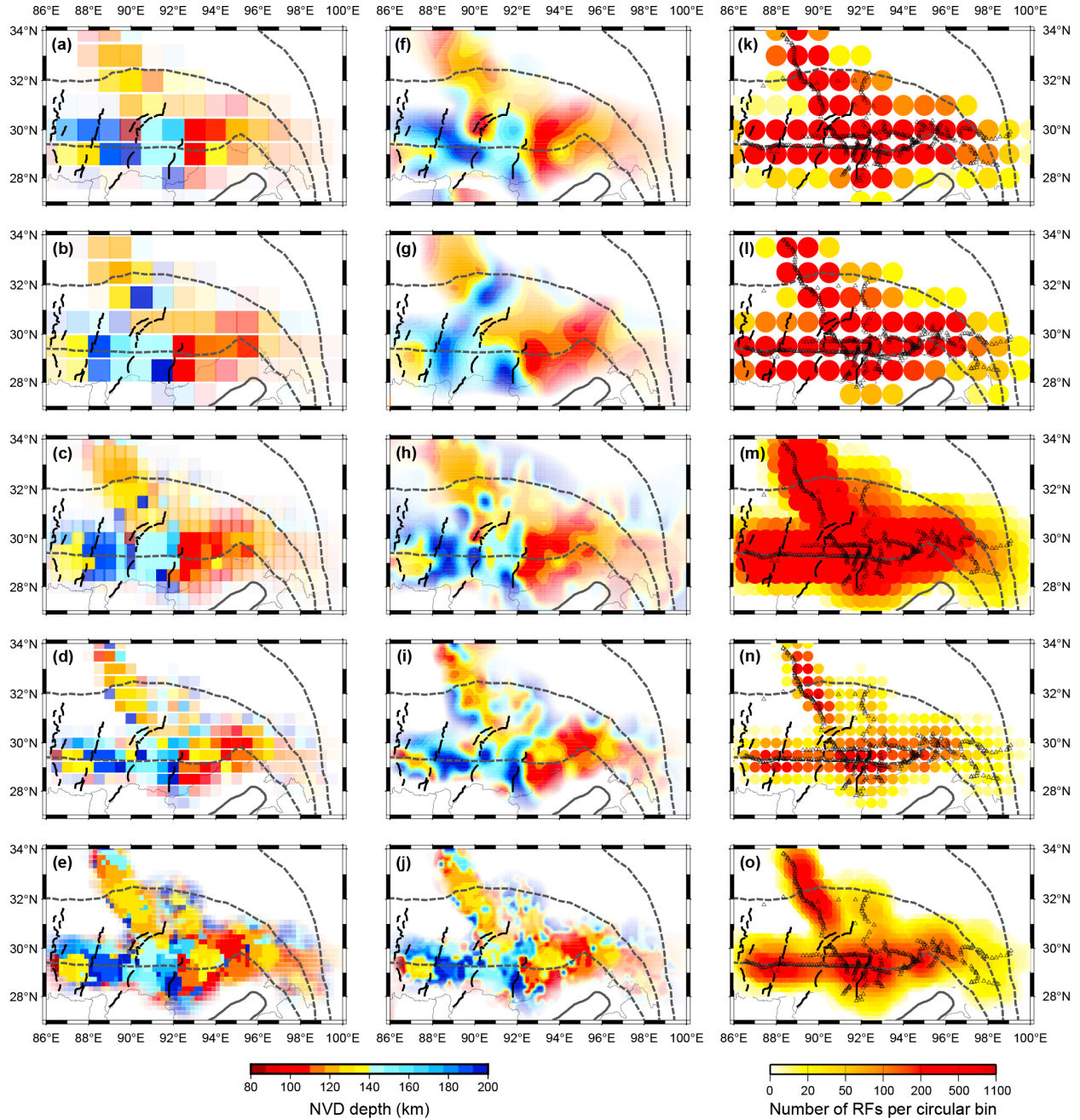
Fig. S2. Left column, a–e: Map of auto-picked negative-velocity gradient (NVG) depths determined using the IASP91 earth model for (a) 1°-radius circular bins spaced at 1°; (b) 1°-radius bins, with each bin center shifted 0.5° east relative to (a); (c) 1°-radius bins spaced at 0.5°; (d) 0.5°-radius bins spaced at 0.5°; (e) 0.5°-radius bins spaced at 0.2°. Middle column, f–j: Same as a–e, but map of NVG depths is smoothed. Right column, k–o: Number of SRFs per circular bin, overlain by seismic stations (black triangles) used in our study. In left and middle columns, intensity of color is proportional to the number of SRFs averaged in each bin.
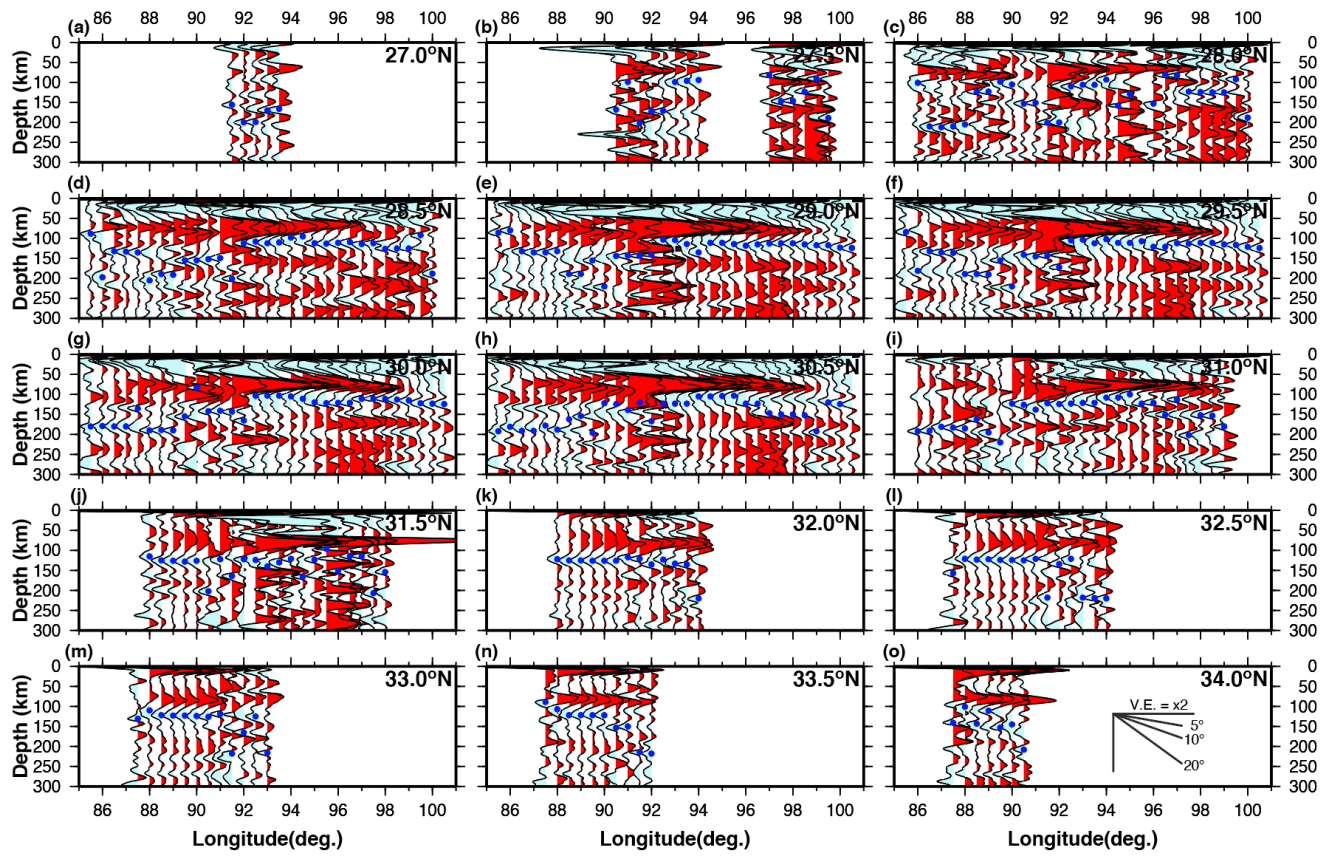
Fig. S3. Record sections across Fig. 2a (1° bins) plotted along 15 latitudinal profiles.
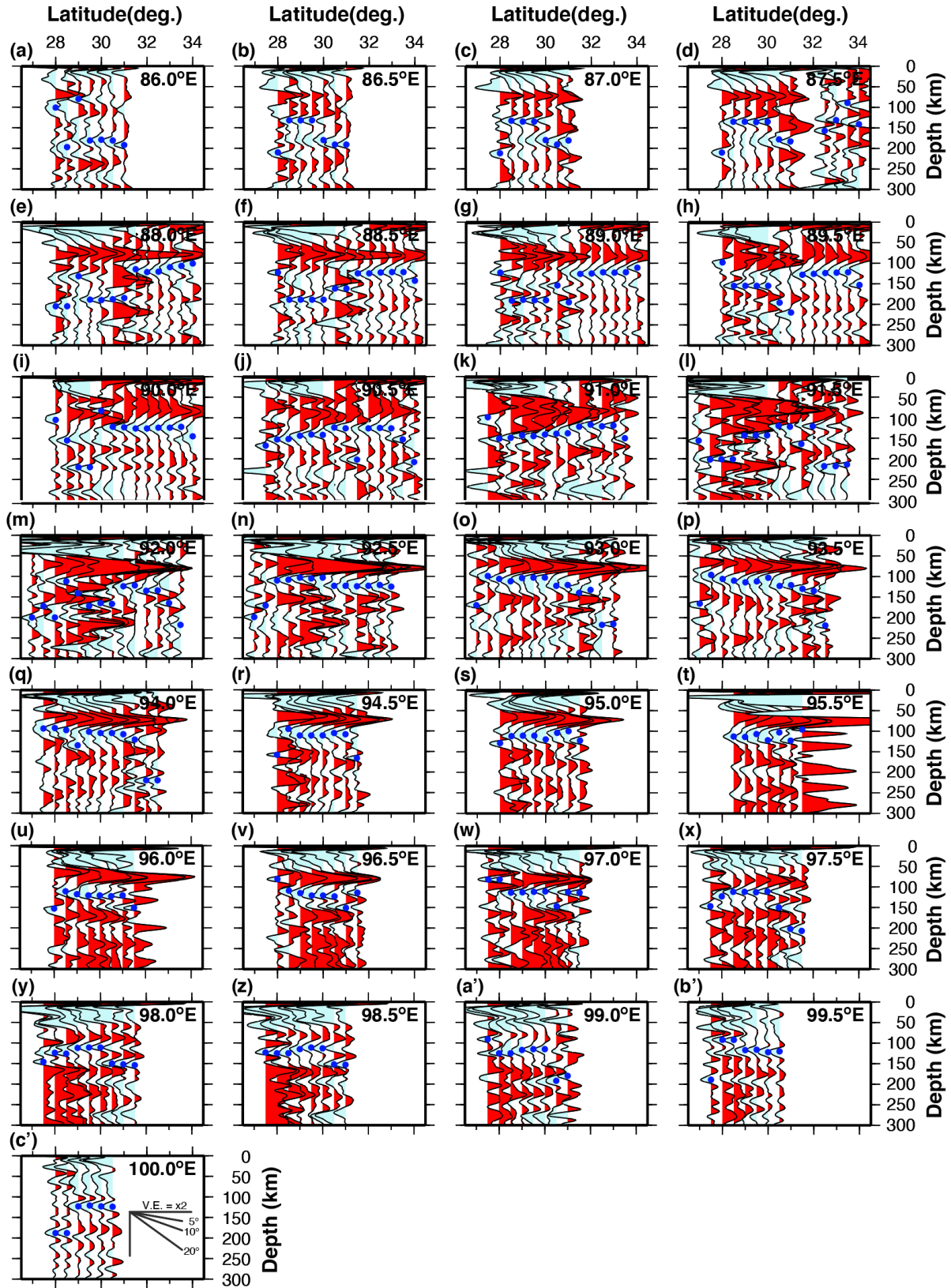
Fig. S4. Record sections across Fig. 2a (1° bins) plotted along 29 longitudinal profiles.
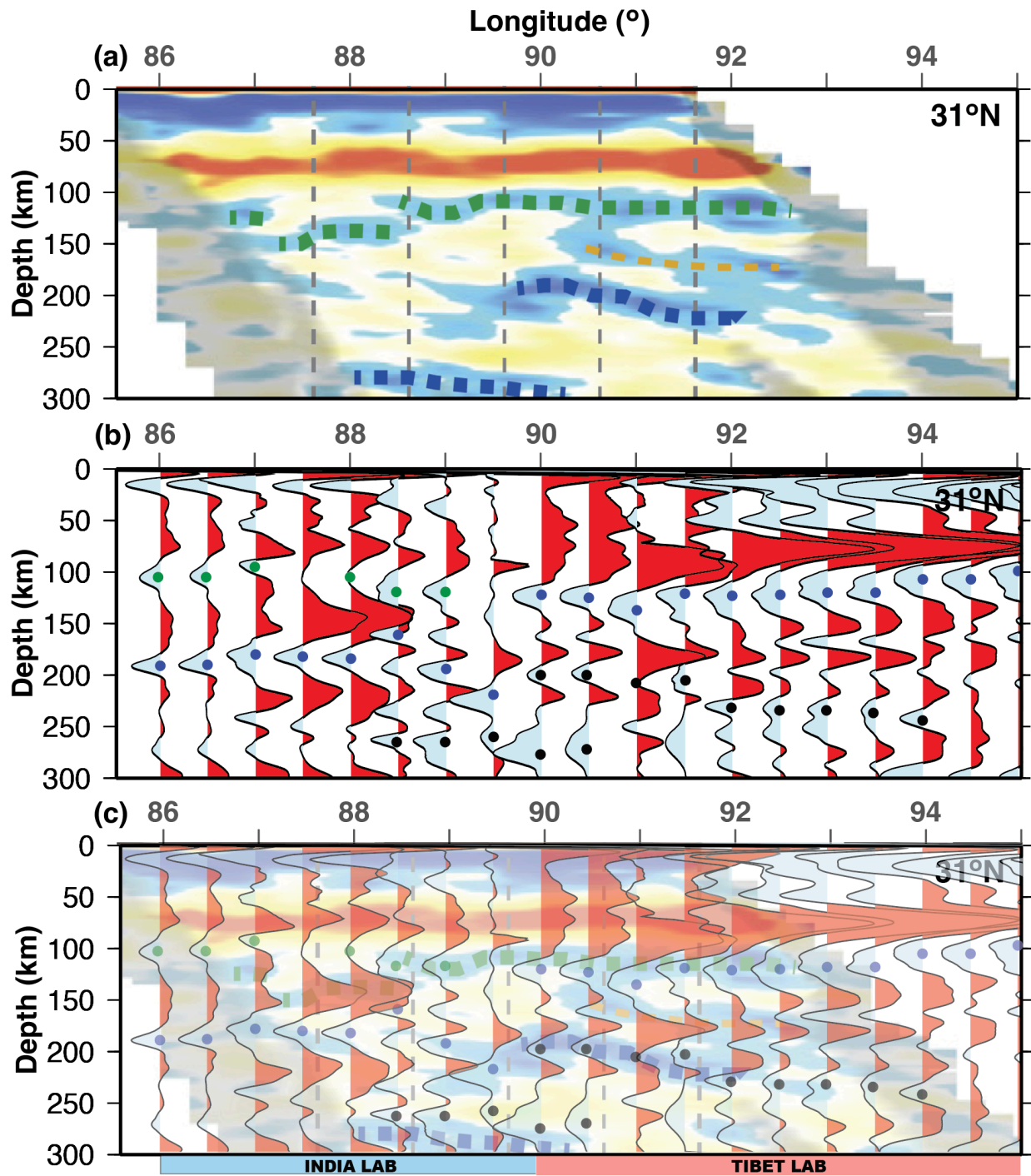
Fig. S5. Comparison of SRF images from reference Liu et al. (2020) and this paper along 31°N, using non-overlapping seismic datasets (no data are in common between these two studies). (a) SRF image along 31°N (Liu et al. (2020), their figure 2d) shows their subjective interpretation of different negative polarity phases, as many as three on a single trace, and no indication of why some negative polarities are interpreted and others ignored. "The dark green dashed lines indicate

the Tibetan LAB, the blue dashed lines indicate the Indian LAB, and the thin orange dashed lines indicate an uncertain discontinuity. The CCP images were smoothed with a bin of 20 km along the profiles, 1 km in vertical dimension and 70 km in width. In the CCP images, "regions with stacked numbers of SRFs larger than 100 were highlighted" (Liu et al., 2020). (b) Our equivalent profile (Fig. 2d). As in Fig. S1, the largest negative amplitude on each trace from 80–220 km is highlighted with a blue dot, and other strong negative amplitudes possibly correlative with interpretations in (a) are highlighted with green and black dots. (c) The two sections are overlain to show the very close correspondence between picked negative phases, even though no seismic data are in common between the two sections. Liu et al. (2020) used only data from the "SANDWICH" and "31N" arrays, neither of which was available to this study.
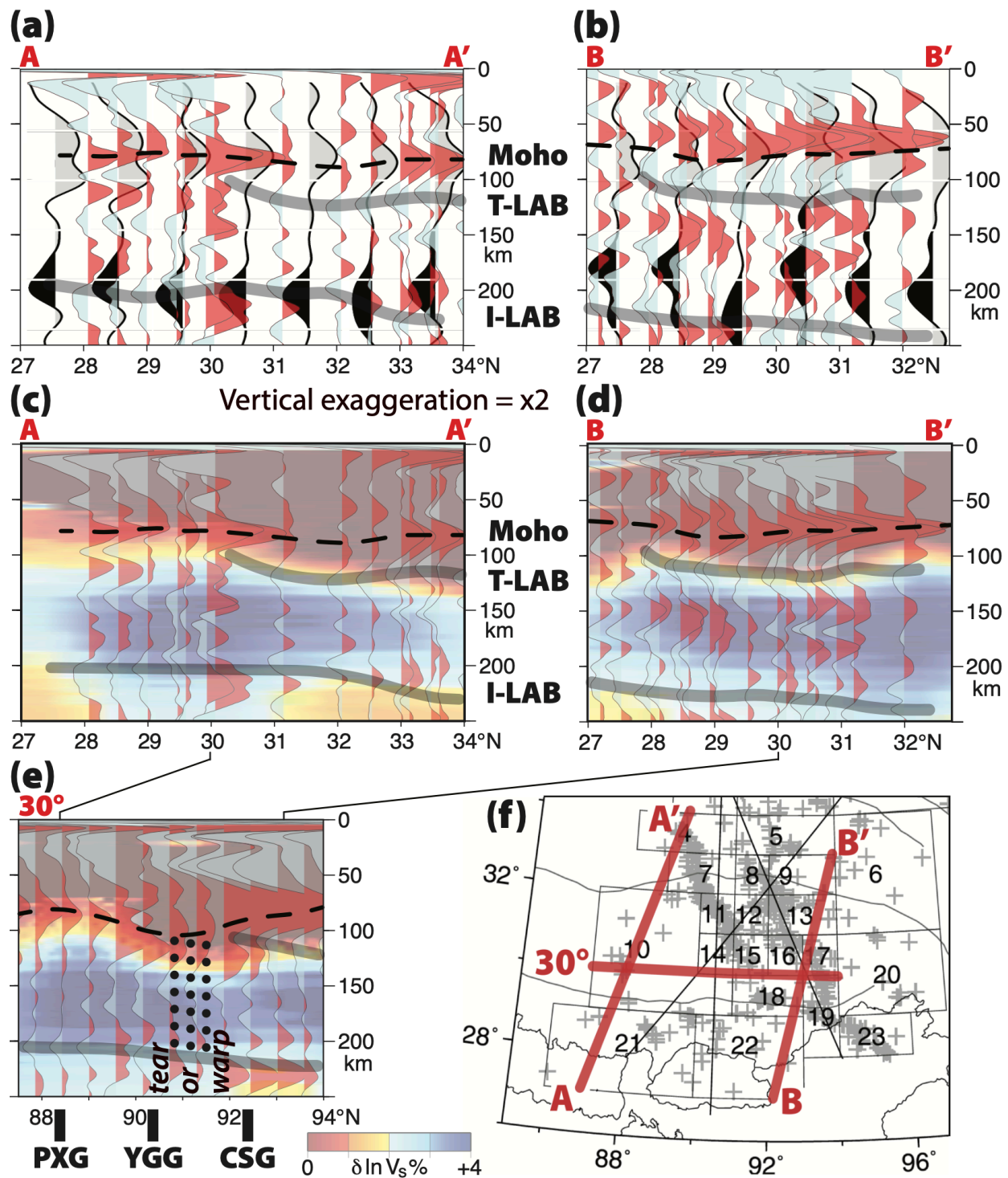
Fig. S6. SRF profiles along (a, c) profile A-A', (b, d) profile B-B', and (e) 30°N, located in (f) map (Kumar et al., 2006) and in Fig. 4a. (a, b): our higher-frequency SRFs overlain by low-frequency SRFs (Kumar et al., 2006) that show large black pulses interpreted as I-LAB, and overlain by our smoothed geological interpretation of Moho, T-LAB and I-LAB. Low-frequency

SRFs are regionally averaged in numbered boxes shown on (f) map (Kumar et al., 2006) scaled to try to match datum and velocity models. (c, d, e): profiles from Fig. 4a, but shown with 2x vertical exaggeration (as in Fig. 2) and without the perspective view of Fig. 4. Our SRFs overlain on seismic tomography model (Chen et al., 2017) plotted as % dln Vs (i.e. $\ln(Vs_{observed})$ minus $\ln(Vs_{average\ at\ depth})$) compared to average over Tibet and surrounding regions (65–110°E, 15–45°N, i.e. Fig. 1 of Chen et al. (2017)) (blue: higher wavespeed than average at 150-km depth, inferred to be cratonic mantle lithosphere; red: slow-wavespeeds below Moho, inferred to be Neogene mantle lithosphere red: slow-wavespeeds below Moho, inferred to be Neogene mantle lithosphere). In (e) 30°N profile the Moho is drawn to match the equivalent PRF profile of ref. 17, and dotted lines show inferred location of a slab tear or warping, spanning the region of the Yadong-Gulu and Cona-Sangri grabens.
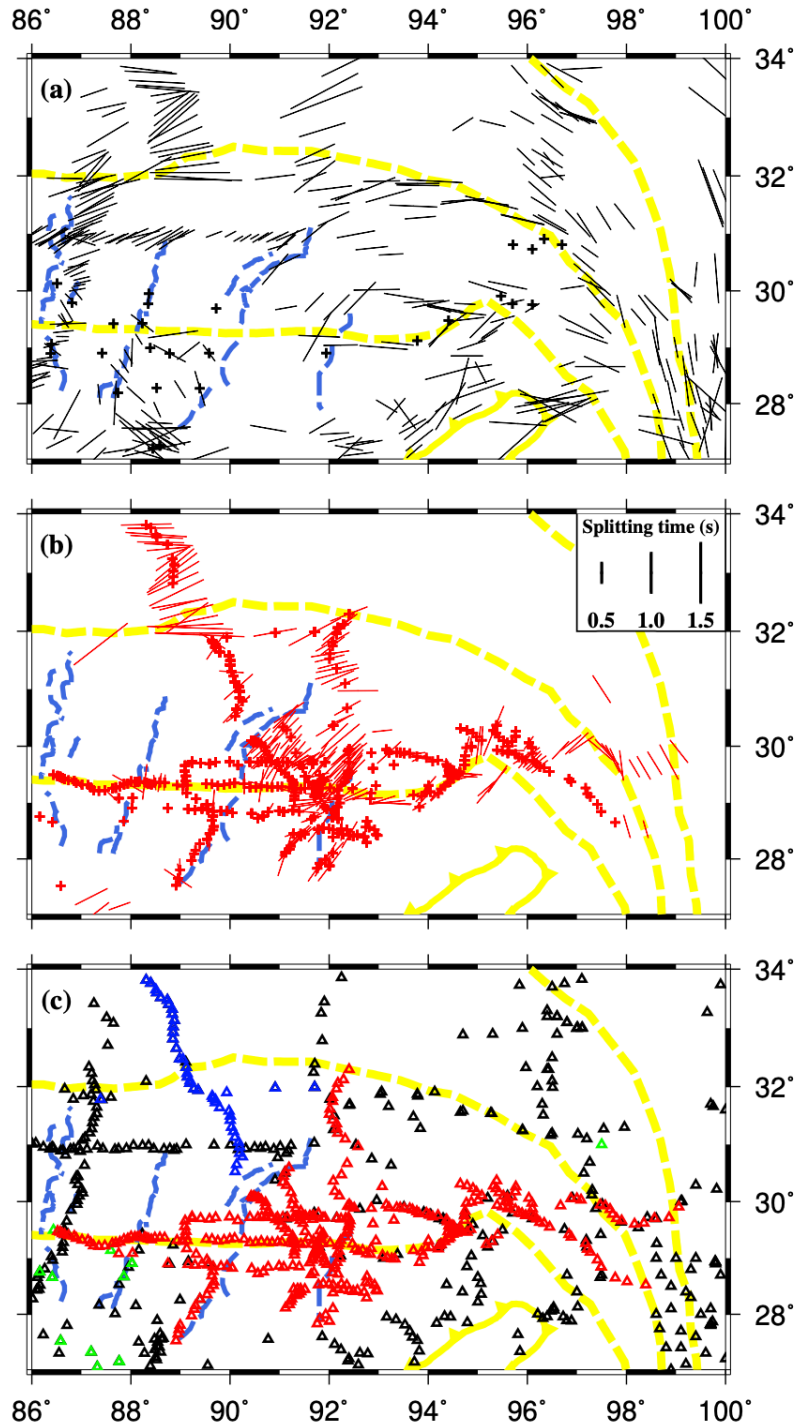
Fig. S7. SWS results, fast polarization directions have length scaled to split time. Stations with nulls (no measurable anisotropy) are shown by crosses. (a) FPDs and nulls from 25 previous publications (Table S1). (b) FPDs and nulls from our measurements (Table S2). (c) Station locations grouped or color-coded by the experiment or data-source (black: stations used in previous SWS publications; blue: INDEPTH-3; red: GANGDESE; green: IRIS.
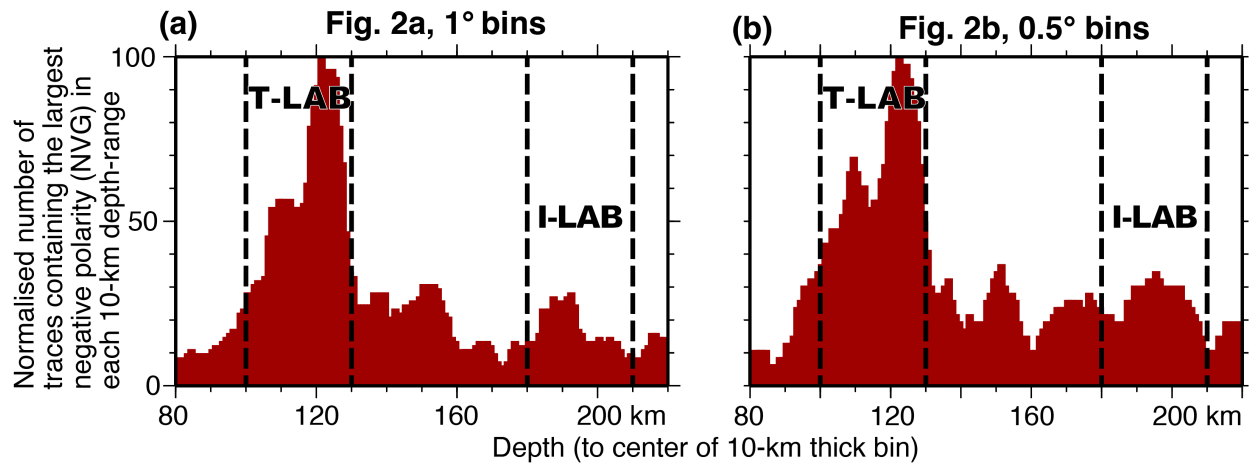
Fig. S8. Histogram of relative abundance of highest-amplitude negative converters in each 10-km depth range, measured in bins successively offset by 1 km, for Figs. 2a (1° bins) and 2b (0.5° bins). Large peak at 100–130 km depth represents T-LAB; a much weaker mode at 180–210 km depth corresponds to I-LAB.
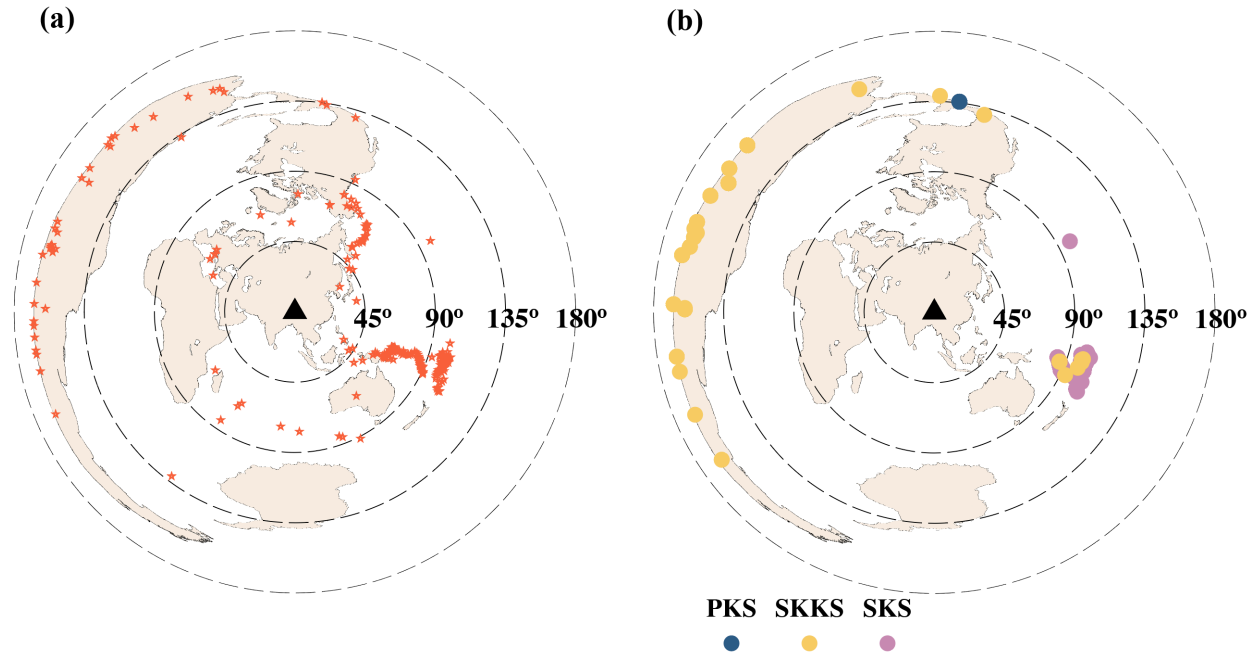
Fig. S9. Azimuthal equidistant projection map showing the center of the study area (black triangle) and distribution of (a) 244 events used in the SRF study (stars) and (b) 95 events used in the SWS study (circles). In (a) each star corresponds to an earthquake from which an SRF measurement was made at one or more stations. In (b) each circle corresponds to an earthquake from which an SWS measurement was made at one or more stations, but only the events analyzed by us, not the events for station-average SWS compiled from the literature.
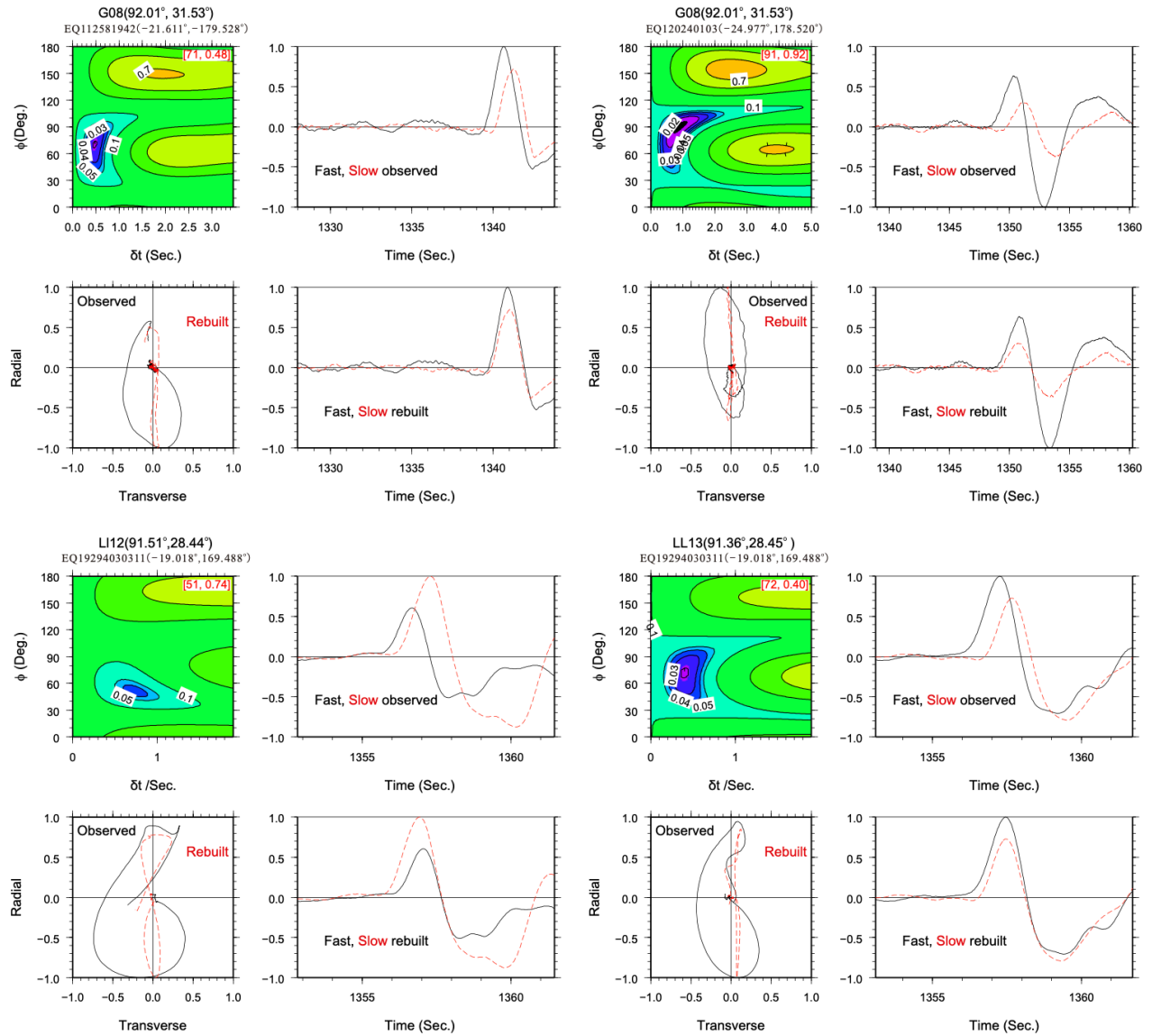
Fig. S10. Examples of shear-wave splitting measurements on four individual earthquake-receiver pairs. Top row: two different earthquakes recorded at the same station G08: note the significant differences in the splitting parameters from the two events due to different back-azimuth hence different piercing-point location. Bottom row: same earthquake recorded at adjacent stations (LL12, LL13).

Within each four-part group representing a single earthquake-receiver pair: Top left: contour map of the normalized energy on the corrected transverse component in the XKS time window from a grid search over all possible fast polarization directions (f) and plausible splitting times (dt). The minimum transverse energy (in the top-left block: 71°, 0.48 s) indicates the optimal f and dt. Bottom left: original (black) particle motions in the radial/transverse co-ordinate system and

corrected (red) particle motions after rotation into the co-ordinate system parallel and perpendicular to the FPD. Top right: fast (black) and slow (red) waveforms in the radial/transverse co-ordinate system with no time correction, corresponding to the black line in the particle-motion hodogram, bottom left. Bottom right: fast (black) and slow (red) waveforms in the radial/transverse co-ordinate system after time delay correction.

Supplementary References

Wittlinger, G. *et al*. Lithospheric and upper mantle stratifications beneath Tibet: New insights from Sp conversions. Geophys. Res. Lett. **31**, L19615. https://doi.org/10.1029/2004GL020955 (2004).